Journal of Environmental Science, Ecology & Chemistry

JESEC, 1(3), 154-176, 2025
https://doi.org/10.58985/jesec.2025.v01i03.15
ISSN (Print): 0000-0000

Research Article

Electrochemical detection of quinolone antibiotics in water using Prussian blue-modified graphite electrodes

Silvina Vanesa Kergaravat[1, 2*], Fernanda Albana Marchesini[3] and Silvia Raquel Hernández[1*]

1. Laboratorio de Sensores y Biosensores, Facultad de Bioquímica y Ciencias Biológicas, Universidad Nacional del Litoral, 3000 Santa Fe, Argentina.
2. Consejo Nacional de Investigaciones Científicas y Técnicas (CONICET), CCT Santa Fe, Argentina.
3. Instituto de Investigaciones en Catálisis y Petroquímica, INCAPE (UNL-CONICET), Facultad de Ingeniería Química, Santiago del Estero 2829, 3000 Santa Fe, Argentina.

Article Information
Received: 01 April 2025
Revised: 14 August 2025
Accepted: 14 August 2025
Published: 17 December 2025

Academic Editor
Prof. Dr. Giuseppe Oliveto

Corresponding Authors
Prof. Dr. Silvina Vanesa Kergaravat
E-mail: skergaravat@fbcb.unl.edu.ar
Tel: +54 342 4575 206/209/215/216 (interno (0)187)
Prof. Dr. Silvia Raquel Hernández
E-mail: shernand@fbcb.unl.edu.ar

Keywords
Quinolone antibiotic, electrochemical detection, amperometry, Prussian blue, water.

Abstract

A screening method for detecting quinolone antibiotics using an amperometric sensor was developed. The sensor was built by modifying a cylindrical graphite-epoxy composite (cGECE)-based electrode with Prussian Blue (PB). The PB-cGECE sensor was characterized by X-ray diffraction, optical microscopy, laser Raman microscopy, visible (VIS) and fourier transform infrared (FTIR) spectroscopies, and cyclic voltammetry. The sensor exhibited excellent electrocatalytic behavior in the oxidation of quinolones compared to the bare graphite electrode. The electrochemical parameters, including the electroactive surface coverage, transfer coefficient, and standard heterogeneous rate constant, were obtained from cyclic voltammograms. Calibration curves for the seven quinolones were obtained by amperometric detection on a PB-cGECE sensor with limits of detection of 3, 20, 30, 10, 45, 35, and 30 μg L^{-1} for ciprofloxacin, danofloxacin, enrofloxacin, marbofloxacin, norfloxacin, ofloxacin, and sarafloxacin, respectively. Ciprofloxacin was selected as a representative congener of the quinolone family in the screening evaluation of the water sample using a detection capability (CCβ) of 4.0 μg L^{-1} to classify the samples as compliant or non-compliant. The method complies with commission implementing regulation (EU) 2021/808 for screening techniques and demonstrates good precision, selectivity, and applicability in aqueous environmental matrices with a total analysis time of 5 min.

1. Introduction

Quinolones are an important class of antibiotics widely used to treat gastrointestinal and respiratory tract infections [1]. They have long been used in human and veterinary medicine, and are therefore ubiquitous in the environment [2]. The main problem associated with quinolone residues in water is the development of antibiotic resistance in intestinal bacterial populations [3, 4]. Many analytical methods

have been developed for determining quinolone concentrations, including high-performance liquid chromatography (HPLC) with fluorescence detection [5], HPLC coupled with mass spectrometry [6], immunoassays [7], capillary electrophoresis [8], and electrochemical methods [9]. Among electrochemical techniques, amperometry is widely used because it is considered the best technique for developing portable and digital sensors with good sensitivity for the detection of organic molecules [10].

Prussian blue, an inorganic pigment, was first synthesized in the 18th century and has since been used in various applications. Within our scope of interest, it is used as an electrode modifier, since PB exhibits a high catalytic efficiency, which is comparable to that of biological catalysts [11]. The catalytic efficiency of PB is attributed to its zeolitic lattice nature with a large open metal-organic framework that functions as a three-dimensional catalyst [11, 12]. Moreover, this material allows a significant decrease in the applied electrode potential, reducing the probability of electrochemical interference due to the potential presence of electroactive substances in the sample matrix. PB thin films on the electrodes can be prepared by the electrodeposition or chemical deposition of Fe^{3+} and $Fe(CN)_6^{3-}$ [13]. PB films have been used to improve the electrochemical performance by modifying the electrodes of different natures such as glassy carbon electrodes modified with surfactants [14] or multi-walled carbon nanotubes [15], graphite screen-printed electrodes [16], graphene electrodes [17], and glass and indium tin oxide electrodes modified with nanocomposite [18] for the detection of hydrogen peroxide, bisphenol B, uric acid, hydrogen peroxide, and ibuprofen, respectively.

In this study, the thin film of PB was chemically deposited on c-GECE, and the ability of PB-cGECE sensors to catalyze quinolone oxidation was demonstrated. The PB particles synthesized from $K_3[Fe(CN)_6]$: $FeCl_3$ (1:1) mixtures and the PB-cGECE sensor were characterized by X-ray diffraction (XRD), optical and laser Raman microscopies, VIS, fourier transform infrared (FTIR) spectroscopies, and cyclic voltammetry. Electrochemical parameters like electroactive surface coverage, transfer coefficient, and standard heterogeneous rate constant were determined. The optimization of experimental conditions is also presented and discussed, and calibration curves and internal validation assays of the screening method based on the amperometric quinolone detection in water samples are subsequently performed. Samples were collected from different provinces in Argentina (Santa Fe, Entre Ríos, and Buenos Aires), covering a large area of Las Pampas region. Additionally, various water sources have been used, including groundwater, rivers, streams, surface water, and lagoons. This is the first time that quinolones have been electrochemically detected on PB-modified electrodes.

2. Materials and methods

2.1. Instrumentation

Epsilon BAS Bioanalytical Systems Inc. voltammetric analyzer (West Lafayette, Indiana, USA) was used for the electrochemical determination. The electrochemical cell was comprised three independent electrodes: a platinum wire as an auxiliary electrode, a ($Ag/AgCl_3$ mol L^{-1} NaCl) silver/silver chloride electrode in 3 mol L^{-1} NaCl solution as a reference electrode (RE) (Orion 92-02-00), and a graphite-epoxy cylindrical composite electrode (cGECE) as a working electrode.

The effective area of the working electrode was determined by chronoamperometry using a 2 mmol L^{-1} potassium ferricyanide $K_3[Fe(CN)_6]$ solution containing 1 mol L^{-1} KCl. The ferrocyanide diffusion coefficient is 6.2×10^{-6} cm^2 s^{-1} [19]. The potential was stepped from 0.050 to 0.500 V for 30 s. The effective area calculated using the Cottrell equation [20] was found to be 0.24 ± 0.03 cm^2 (CV = 12.5%, n = 16).

The morphology and structure of the synthesized PB particles were analyzed through a series of characterizations. For this purpose, samples based on different concentrations of $K_3[Fe(CN)_6]$: $FeCl_3$ (1:1) mixtures were analyzed. The washed and dried products of each sample were conditioned for each study technique. The structural characteristics (crystalline phases) of PB were studied by XRD using a Panalytical Empyrean instrument (40 kV and 45 mA,

using Cu Kα radiation, λ = 1.5406 Å). Measurements were taken in the range of 2θ = 10°- 70° at a scan rate of 1° min^{-1}. The optical microscopy study was performed using a Leica S8APO optical microscope, and the micrographs were taken with a Leica LC3 camera and processed using LAZ EZ software. On the other hand, the Raman spectra of powder-supported samples were recorded using a Horiba JOBIN YVON LabRAM HR spectrometer, equipped with a 532.13 nm excitation laser operating at 30 mW power. The infrared spectroscopy was carried out using a Shimadzu IR Prestige-21 Spectrophotometer with a resolution of 4 cm^{-1}. The dried product of each mixture was homogenized with KBr and then dried at 40°C under a 300 mbar vacuum for 48 h. Thus, the resulting mixture was then pressed into pellets and analyzed. VIS spectral images of the mixtures were obtained by a UV-Vis spectrophotometer from 600 to 1000 nm (DLAB SP1000).

An Agilent Technologies 1100 Series Liquid Chromatograph (HPLC) with a quaternary pump, degasser, seal washer, column thermostat, C18 column, and UV-visible diode array detector (DAD) was used for the reference method. SCIENTECH USA SP 150 microprocessor-controlled digital analytical balance was used. The pH of buffer solutions was measured using a combined glass electrode connected to a digital pH meter (ORION, model 720A).

2.2. Reagents and solutions

Ciprofloxacin (CIP) was kindly donated by the Roemmers Lab. (Buenos Aires, Argentina) while amoxicillin, azithromycin, danofloxacin (DAN), doxycycline, enrofloxacin (ENR), marbofloxacin (MAR), norfloxacin (NOR), ofloxacin (OFL), rifampicin, sarafloxacin (SAR), sulfadimethoxine, and sulfamethoxazole were purchased from Sigma-Aldrich (Buenos Aires, Argentina). Stock standard solutions of the antibiotics were prepared in methanol. Working standard solutions (10 000 μg L^{-1}) were prepared by serial dilution of the stock standard solution with high-purity water. Ferric chloride hexahydrate (97%), potassium ferrocyanide (99%), potassium ferricyanide (99%), potassium chloride (99%), and hydrochloric acid (37%) were of American Chemical Society (ACS) reagent grade. The supporting electrolyte consisted of a 0.1 mol L^{-1} working buffer solution of acetic acid (99.5%, Cicarelli) and sodium acetate (99% pro-analysis ACS, Cicarelli) in 0.1 mol L^{-1} KCl, pH 5.0. Welchrom SPE cartridges were purchased from D'Amico Sistemas. All other reagents (high-purity surfactants and solvents) and laboratory supplies were supplied by Cicarelli and Sigma Aldrich-Merck subsidiaries in Argentina. All aqueous solutions were prepared with Milli-Q water (Millipore Inc., Ω = 18 MΩ cm).

2.3. Preparation of PB-cGECE sensor

The cGECEs were developed in our laboratory and have been used previously [21]. Briefly, a copper tube closed at its ends with plates of the same material was inserted into a cylindrical acrylic sleeve body. A connecting wire was soldered to one end of the tube, and the other end of the tube was glued to the acrylic body by adding a few drops of chloroform at the bottom, leaving 2 mm free at the top of the tube. The mixture was dried for 5 min at room temperature (Scheme 1, step a). To prepare the composite, graphite powder and epoxy resin were hand-mixed in a 1:4 (w/w) ratio [22, 23], and the composite was placed in a cavity of 2 mm at the top. The geometric area of the c-GECE was 0.12 cm^2. The electrodes were cured at 60 °C to obtain a rigid composite (Scheme 1, step b).

Before use, the electrode surface was renewed by a simple polishing procedure. For the cGECE modification step with PB, chemical deposition was carried out, and a drop (50 μL of the total volume) of a precursor liquid mixture was deposited on the working electrode area. This precursor was prepared by mixing 25 μL of 0.05 mol L^{-1} of potassium ferricyanide ($K_3[Fe(CN)_6]$ and 25 μL of 0.05 mol L^{-1} of ferric chloride ($FeCl_3$), both in 0.01 mol L^{-1} of HCl with 0.10 mol L^{-1} of KCl. Subsequently, the electrodes were gently stirred on an orbital shaker for 10 min. After this step, the electrodes were rinsed twice with 50 μL of 0.01 mol L^{-1} of HCl and finally, to obtain a more stable and active PB layer, the PB-cGECE sensors were cured for 30 min in an oven at 60 °C (Scheme 1, step c).

2.4. Electrochemical characterization of PB-cGECE sensor

The electrochemical behavior of PB on cGECE and the voltametric investigation of PB-cGECE sensors were

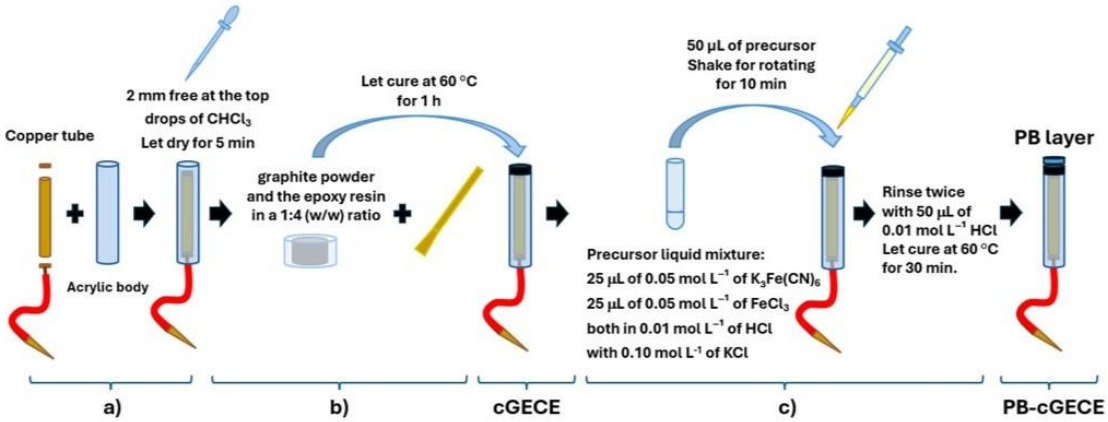

Scheme 1. Steps involved in the preparation of the PB-cGECE sensor.

carried out using a typical three-electrode cell in a buffer at pH = 5.0. The response was obtained by cyclic voltammetry (scan rate 0.1 V s^{-1}) in the range from -1.0 to 1.2 V.

The surface coverage (Γ) was estimated from the under PB/ Prussian White (PW) couple area, recorded during the cyclic voltammetry measurements at a scan rate of 0.05 to 1 V s^{-1} and considering the surface redox valence equal to unity [18] from equation 1:

$$Q = n \times F \times A \times \Gamma \quad (1)$$

where Q is the charge under the peak (C), n is the number of electrons, A is the effective area (0.24 cm^2), and Γ is the surface coverage (mol cm^{-2}). Also, the current intensities (CI, A) were plotted against the scan rates (v, V s^{-1}) at different surfaces (Γ) according to equation 2:

$$I = \left(\frac{n^2 \times F^2}{4 \times R \times T}\right) \times \Gamma \times A \times v \quad (2)$$

The apparent standard heterogeneous rate constant (k°) was calculated from the Tafel diagrams according to the method described by Laviron [24]. The anodic (α_a) and cathodic (α_c) transfer coefficients and k° were calculated from the slopes and intercepts, of the Ep *vs.* log (v) plots at different surface coverages. The slopes of the linear segments have the same mathematical form but with opposite signs, as can be seen in equations 3 and 4 for the cathodic and anodic peaks, respectively.

$$-\frac{2.303 \times R \times T}{\alpha_c \times n \times F} \quad (3)$$

$$\frac{2.303 \times R \times T}{\alpha_a \times n \times F} \quad (4)$$

The value of k° was evaluated from equation 5,

$$k^o = \frac{\alpha_c \times n \times F \times v}{R \times T} \quad (5)$$

where v = 1 V s^{-1} [24].

2.5. Amperometric detection of quinolones in the samples

Quinolones were electrochemically detected on PB-cGECE sensors using amperometry ($E_{applied}$ = 0.95 V *vs.* RE). In the electrochemical cell, the three electrodes were immersed in 2 mL of the working buffer at pH = 5.0. Under stirring, the base current was allowed to stabilize for approximately 1 min and then 50 or 100 µL of the previously conditioned sample was added. The increase in current intensity was related to the quinolone concentration.

2.6. Analytical performance

2.6.1. Calibration curves for quinolones

The curves of the current intensity (µA) *vs.* quinolone concentrations in the range from 25 to 450 µg L^{-1} were obtained by amperometry at $E_{applied}$ = 0.95 V *vs.* RE. In the electrochemical cell, the three electrodes were submerged in 2 mL of working buffer at pH = 5.0, and successive additions of 5 or 10 µL of 10 000 µg L^{-1} quinolones were added while being stirred. The data were analyzed by ordinary least squares (OLS) calibration utilizing MATLAB version 7.6.0. (R2008a) [25, 26]. The limits of detection (LOD) and

quantification (LOQ) were calculated as 3.3 SD/m and 10 SD/m, respectively, where SD is the standard deviation of the blank samples and m is the slope obtained from the calibration curves for each quinolone [27].

2.6.2. Detection capability (CCβ)

The validation of the methodology was performed according to the Commission Implementing Regulation (EU) 2021/808 for the screening method [28]. To calculate the detection capability (CCβ), the quinolones were considered to emerge unregulated in natural water matrices. For unauthorized or prohibited pharmacologically active substances in a medium, a maximum β (or false-conforming) error of 5% must be guarantee. Therefore, 20 assays were performed with a previously defined minimum concentration, and CCβ was calculated according to equation 6:

$$CC\beta = ASC + 1.64\ (SD_{ASC}) \quad (6)$$

where ASC is the average of the "analyte screening concentration" and the SD_{ASC} is the corresponding standard deviation. To predetermine the minimum concentration, replicates of low-concentration quinolone solutions were tested. The ASC was the concentration that differed from that of the blank samples and guaranteed a β error of < 5%. Finally, the CCβ value was used as a cut-off level for the screening method to classify the water samples as non-compliant (> CCβ) and compliant (< CCβ).

2.6.3. Selectivity

To evaluate this characteristic of the method, two approaches were followed: 1) a congener study and 2) an interference study as described below.

2.6.3.1 Congener study (CS)

To evaluate the method's ability to distinguish between CIP and other quinolone antibiotics (danofloxacin, enrofloxacin, marbofloxacin, norfloxacin, ofloxacin, and sarafloxacin), CS% was calculated according to equation 7:

$$CS\% = \left(\frac{m_{ciprofloxacin}}{m_{quinolone\ congener}}\right) \times 100 \quad (7)$$

Where m is the slope of the individual calibration curve.

2.6.3.2. Interference study (IS)

Potentially interfering compounds belonging to other families of veterinary antibiotics frequently present in water samples were studied by recovery assays at three CIP levels (50, 100, and 150 μg L^{-1}). The antibiotics assayed as interferents at 150 μg L^{-1} were doxycycline (tetracycline family), amoxicillin (β-lactam family), azithromycin and rifampicin (macrolide family), and sulfadimethoxine and sulfamethoxazole (sulfonamide family).

2.7. Water samples

The water samples were collected according to 29012 (-4, -5, -6, and -11) IRAM norms from Argentina [29-32] and stored in plastic containers at 4 °C in the dark. The samples were collected from groundwater (1) and river water (2) from Santo Tome, Santa Fe, Argentina; stream water (3), (4), (5) and lagoon (6) from Sauce, Entre Ríos, Argentina; stream water (7) from Partido de la Costa, Buenos Aires, Argentina; superficial water (8) from Susana, Santa Fe, Argentina; superficial water (9) from Rafaela, Santa Fe, Argentina; and superficial water (10) from San Vicente, Santa Fe, Argentina. For electrochemical analysis, the samples were preconditioned by adding a volume of concentrated buffer solution (acetic acid/acetate) to adjust the pH and ionic strength to the values corresponding to the working buffer. In all cases, the added volume did not exceed 10% (v/v). For the analysis of the samples using the reference method, the procedure reported by da Silva and Oliveira [33] was followed, using CIP as the reference congener of the quinolone family.

3. Results and discussion

3.1. Characterization of PB-cGECE sensor

3.1.1. Characterization of PB particles

The morphology and structure of the synthesized PB particles were analyzed through a series of characterizations. For this purpose, three suspensions (S_1, S_2, and S_3) were prepared by mixing the precursors $K_3[Fe(CN)_6]$ and $FeCl_3$ at 0.010 mol L^{-1} (in a 1:1 ratio), both dissolved in 0.100 mol L^{-1} KCl as a supporting electrolyte. The three resulting suspensions were: S_1 (0.010 mol L^{-1}), S_2 (0.020 mol L^{-1}), and S_3 (0.050 mol L^{-1}). It is known that the formation of PB crystallizes in a face-centered cubic (FCC) structure with Fm-3m

symmetry [34-36]. Fig. 1 shows the X-ray diffractograms of the freshly deposited material on the support. Distinctive diffraction signals corresponding to the support were evident in all solutions. The most representative diffraction peaks of PB under Cu Kα radiation (λ = 1.5406 Å) are listed in Table 1.

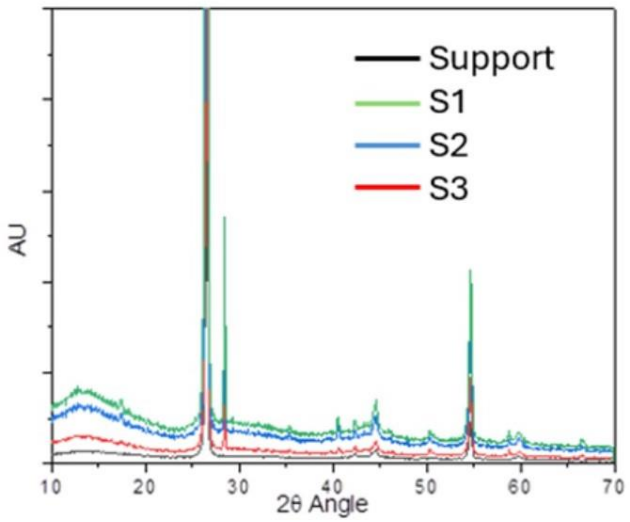

Figure 1. X-ray diffractograms of the fresh deposited material, Cu Kα radiation (λ = 1.5406 Å), 2θ = 10°- 70° at a scan rate of 1° min^{-1}.

Table 1. Miller indices and crystallites sizes.

Concentration (mol L^{-1})	Assigned Planes	2θ Angle	Crystallite size (nm)
S_1: 0.010	(200)	17.4	22.2
S_2: 0.025	(200)	17.4	24.6
S_3: 0.050	(200)	17.4	25.8

These peaks were observed in the diffraction patterns of the deposited suspensions (colored curves) and were absent in the unmodified support (black curve), confirming the presence and growth of the PB phase with increasing precursor concentration. The black curve (bare electrode or support) shows a largely amorphous profile or signals from a different crystalline phase, lacking the characteristic reflections of the PB. In contrast, the suspensions deposited and generated from precursors with increasing concentrations (S_1, S_2, and S_3) exhibited characteristic peaks of PB. At a higher precursor concentration (S_3 suspension), crystalline PB was obtained with a characteristic cubic morphology and distinct optical birefringence, observed by optical microscopy in the form of small crosses. The presence of these anisotropic patterns is attributed to the radial symmetry in the aggregated crystals, a phenomenon commonly reported in the literature as indicative of PB's specific growth habits under acidic or slightly acidic conditions.

The crystallite size was estimated using the Debye–Scherrer equation [37]: $D = (0.9\,\lambda)/(\beta \cos\theta)$, where D is the crystallite size, 0.9 is the shape factor, λ is the X-ray wavelength (1.5406 Å), θ is the Bragg angle at maximum intensity, and β is the full width at half maximum (FWHM) in radians (1 rad = 180/2π). The calculated values for each crystalline phase are listed in Table 1. Increasing the concentration resulted in larger crystallites, a higher crystalline fraction, and improved structural order within the PB phase [36], which are key parameters for enhancing the electrochemical performance of PB-supported graphite electrodes.

Fig. 2 presents optical micrographs of PB crystals synthesized from different suspensions S_1, S_2, S_3, and S_4 (the latter had 0.100 mol L^{-1} of each precursor). The magnifications are shown in the inset to allow the visualization of the different particles present in each sample on the electrode surface (PB-cGECE). The morphological evolution of the material was clearly concentration-dependent and provided insights into the nucleation and growth mechanisms involved in PB crystallization. As shown in Fig. 2a, elongated needle-like structures were observed in the S_1 suspension (10 mM), exhibiting high anisotropy and directional growth. This morphology is typically associated with low supersaturation, which favors slow nucleation and allows directional crystal development. These findings are consistent with previous reports indicating that diluted precursor concentrations promote well-defined, linear crystal growth [38]. In Fig. 2b, the emergence of cross-like morphologies in the S_2 suspension (25 mM) indicates a higher nucleation density and multidirectional crystal growth. These structures often arise from overlapping crystalline domains that grow orthogonally, which is a hallmark of increased supersaturation and more abundant active nucleation

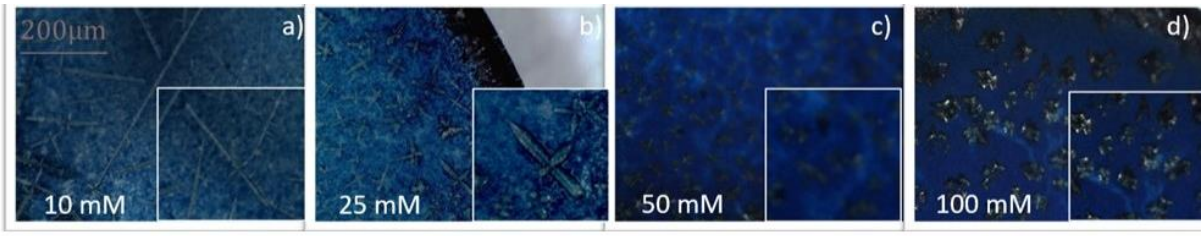

Figure 2. Optical micrograph of PB at different concentrations of S_1, S_2, S_3, and S_4 suspensions. The images were acquired at 8x magnification.

sites [39]. In Figs. 2c and 2d, the morphology shifts dramatically to irregular tetrahedral/star-shaped or cubic crystallites, which are distributed more densely at higher precursor concentrations (S_3 and S_4 suspensions corresponding to 50 and 100 mM, respectively). This suggests a transition to rapid, simultaneous nucleation and limited anisotropic growth due to high supersaturation. Similar trends have been described for PB systems, where increasing the reagent concentration promotes the development of more complex and symmetric architectures, such as the hexapod structures described by Wang *et al.* [40]. As supported by other prior studies, such conditions favor aggregation and the development of more isotropic or polycrystalline morphologies. Therefore, ability to adapt the crystal shape through the concentration of precursors represents a valuable strategy to optimize the electrochemical characteristics of PB.

Raman spectroscopy was used to confirm the presence of PB in the S_1, S_2, and S_3 suspensions (Fig. 3). In all cases, the characteristic C≡N stretching vibration appeared clearly around 2155–2160 cm^{-1}, consistent with the Fe(II)–CN–Fe(III) linkage [41]. A weaker band near 2090 cm^{-1} was also observed, along with a shoulder at approximately 2123 cm^{-1}, which is often attributed to cyanide-related modes. Additional bands between 450 and 620 cm^{-1} correspond to Fe–C stretching, whereas low-frequency vibrations below 350 cm^{-1} are associated with Fe–CN–Fe bending modes. These spectral features are in good agreement with those reported by Moretti and Gervais [41] confirming the identity of the PB structure. All measurements were carried out under low laser power to avoid possible photoreduction or structural changes during acquisition [42].

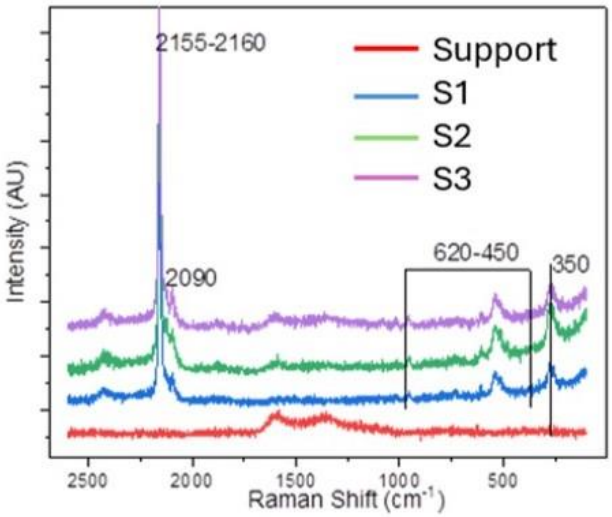

Figure 3. Raman spectra of three samples of PB powder prepared with precursors S_1, S_2, and S_3 suspensions.

Fig. 4 shows the infrared spectra of the synthesized materials. The well-defined absorption bands were consistent with the structure of PB, confirming the identity of the compound. A strong and sharp signal around 2080 cm^{-1} is attributed to the stretching vibration of the C≡N bond in the Fe(II)–CN–Fe(III) coordination environment, which is one of the most characteristic markers of PB [41]. In addition, broad bands centered near 3430 cm^{-1} and 3212 cm^{-1} correspond to O–H stretching vibrations, indicative of water molecules either coordinated to iron centers or retained in the crystal lattice, supporting the presence of a hydrated PB phase [43, 44]. Lower-frequency signals at approximately 596 cm^{-1} and 500 cm^{-1} are assigned to the Fe–C stretching and Fe–CN–Fe bending modes, respectively [44]. A smaller band near 1108 cm^{-1} may be related to residual coordinated species or counterions remaining from the synthesis medium. The absence of additional bands attributable to unreacted $FeCl_3$ or $K_3[Fe(CN)_6]$ suggests that the

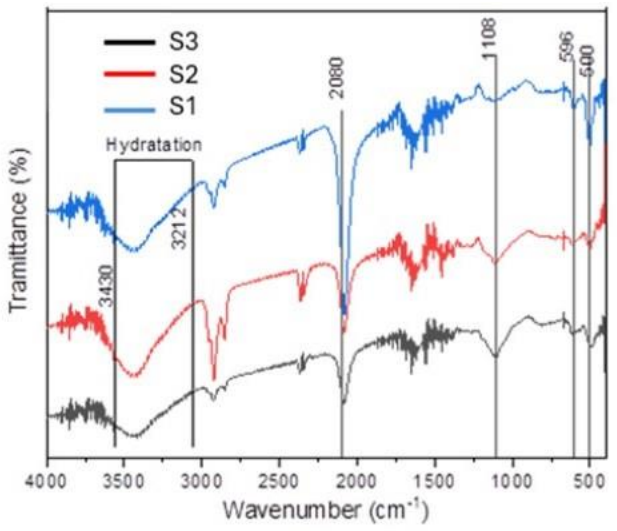

Figure 4. FTIR spectrum of PB powder samples prepared with different concentrations of precursors S_1, S_2, and S_3 suspensions.

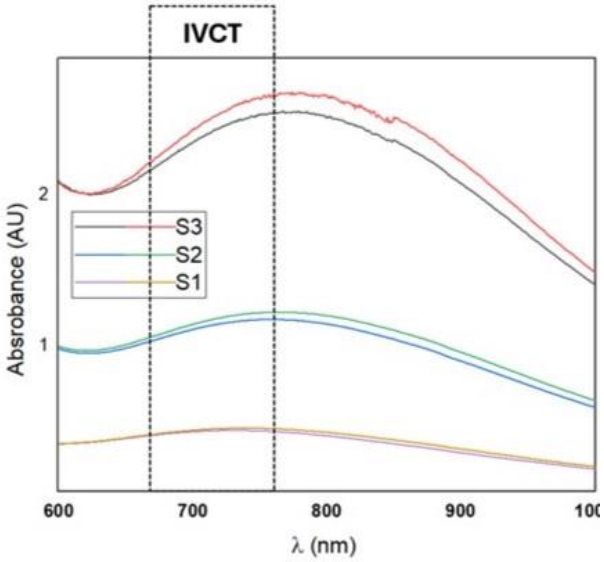

Figure 5. Vis spectrum of PB suspensions prepared at different concentrations of precursors S_1, S_2, and S_3 suspensions scanned against the supporting electrolyte.

reaction proceeded efficiently and selectively under the chosen conditions [34].

Notably a high reproducibility was observed across all preparations. Regardless of the precursor concentration, the FTIR spectra remained consistent in the terms of both peak position and intensity. This uniformity supports not only the structural integrity of the synthesized PB but also the robustness and repeatability of the synthetic method. Such reproducibility is essential for analytical applications and demonstrates the reliability of the protocol used in this study. The VIS spectra of the synthesized suspensions exhibited the characteristic intervalence charge-transfer (IVCT) band of PB, arising from Fe(II)–CN–Fe(III) transitions, with maxima located between 680 and 750 nm (Fig. 5).

The absorbance intensity increased systematically from the S_1 to S_3 suspensions, consistent with the higher solid content and particle loading in the dispersions. Suspensions prepared at higher precursor concentrations displayed a slight red shift and broadening of the IVCT band, features typically associated with larger crystallite dimensions and/or greater particle aggregation [45]. This trend is in full agreement with the increase in crystallite size determined by X-ray diffraction and the morphological evolution observed by optical microscopy.

Spectra collected at 0 and 10 min showed only minor variations in the absorbance (λ_{max}), indicating the good short-term stability of the dispersions [46].

In summary, the combined structural, vibrational, morphological, and optical analyses provide conclusive evidence for the formation of PB at all tested precursor concentrations. The XRD patterns displayed the characteristic reflections of the face-centered cubic structure, with Scherrer analysis revealing increased crystallinity and crystallite size at higher concentrations. Optical microscopy corroborated these findings, showing a morphological evolution from elongated needle-like structures at low concentrations to well-defined cross patterns and polycrystalline aggregates at higher precursor levels, indicative of nucleation and radial growth processes governed by supersaturation. Raman spectroscopy confirmed the expected ν(C≡N) stretching vibrations in the 2155–2160 cm^{-1} range, together with Fe–C and Fe–CN–Fe bending modes consistent with PB's coordination environment, while FTIR showed the C≡N stretching near 2080 cm^{-1}. The corresponding UV-VIS spectra further supported these results, exhibiting an intervalence charge-transfer (IVCT) band at ~700 nm, of which the intensity and position correlated with crystallite growth and aggregation. However, the simultaneous observation of these signatures, together with the crystalline phases detected by XRD, confirmed the

successful and reproducible formation of PB under the employed synthesis conditions. Variations in the precursor concentration emerged as a key factor controlling the crystallinity, particle size, and crystal growth with the appearance and definition of crosses. Subsequently, the electrochemical study was used to select the suspension concentration (S_1, S_2, S_3, and S_4) with the most appropriate characteristics for the construction of PB-cGECE sensor for quinolones detection

3.1.2. Electrochemical properties of PB-cGECE sensor

For achieving the quinolone-sensitive sensors characterized by high stability and electrocatalytic efficiency, and considering a simple preparation scalable to mass production, the cGECE modification step with PB was carried out by chemical deposition based on the slightly modified protocols of Kjeldgaard *et al.* (in synthesis H) [13] and Ricci *et al.* [47], considering the importance of the presence of potassium ions in the preparation [48].

The stoichiometry of the deposited product has been discussed for a long time. Based on powder diffraction patterns, Keggin and Miles [49] distinguished between two different forms of PB: one $KFe^{III}Fe^{II}(CN)_6$ called "soluble" and the other $Fe_4^{III}[Fe^{II}(CN)_6]_3$ called "insoluble". These names do not refer to the water solubility of these forms: both forms are highly insoluble (Kps ≈ 10^{-40}) [49]-but rather indicate the ease with which potassium ions peptize them. Considering these two alternative forms to explain the possible redox processes on the electrodes, Ellis et al. [50] proposed redox reactions starting from the soluble form. The redox processes for "soluble" PB are represented by equations 8a and 8b:

$$KFe^{III}Fe^{II}(CN)_6 + K^+ \rightleftharpoons K_2Fe^{II}Fe^{II}(CN)_6 \quad (8a)$$

Soluble PB" Prussian White − PW (Everitt salt)

$$KFe^{III}Fe^{II}(CN)_6 \rightleftharpoons \frac{2}{3}K^+ + \frac{2}{3}e + K_{\frac{1}{3}}[Fe^{III}(CN)_6]_{\frac{2}{3}}[Fe^{II}(CN)_6]_{\frac{1}{3}} \quad (8b)$$

"Soluble PB" Berlin Green − BG

In contrast, Itaya et al. [51] proposed redox reactions from the insoluble form. Redox processes for "insoluble" PB [51, 52] are represented in the following equations: 9a and 9b:

$$Fe_4^{III}[Fe^{II}(CN)_6]_3 + 4K^+ + 4e \rightleftharpoons K_4Fe_4^{II}[Fe^{II}(CN)_6]_3 \quad (9a)$$

"Insoluble PB" Prussian White − PW

$$Fe_4^{III}[Fe^{II}(CN)_6]_3 + 3A^- \rightleftharpoons 3e + Fe_4^{III}[Fe^{III}(CN)_6A]_3 \quad (9b)$$

"Insoluble PB" Berlin Green − BG

After studying the effect of K concentration on the electrochemical behavior of PB, Cretu et al. [53] assumed that the deposited film was a mixture of soluble and insoluble forms.

Cyclic voltammetry was performed to evaluate the electrochemical behavior of the PB-cGECE sensor. Fig. 6 shows voltammogram 1 (black curve) corresponding to the bare electrode (cGECE) and voltammogram 2, (blue curve) corresponding to the modified electrode (PB-cGECE), both in the working buffer. The cyclic voltammogram of the PB-cGECE sensor presents two redox couplets with corresponding well-defined anodic and cathodic

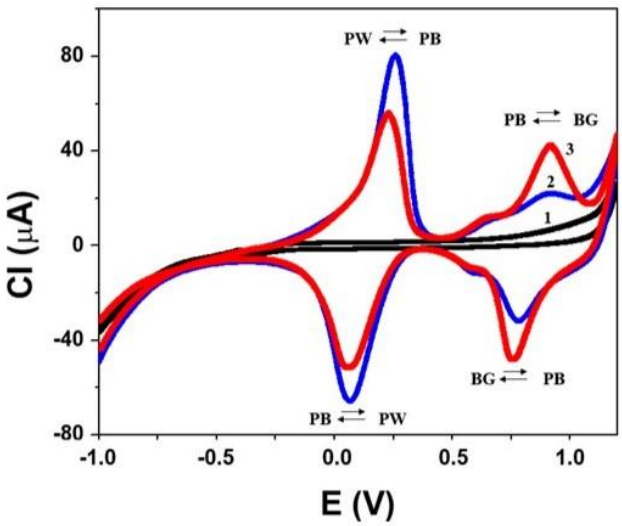

Figure 6. Cyclic voltammograms (CV) recorded on cGECE (1, black curve), PB-cGECE (2, blue curve), and PB-cGECE sensors in the presence of 2 000 μg L^{-1} ENR (3, red curve). Γ = 4 x 10^{-8} mol cm^{-2}. Solutions in 0.1 mol L^{-1} acetic acid buffer with 0.1 mol L^{-1} KCl at pH 5.0. CV parameters: scan rate 0.1 V s^{-1} and potential range from -1.0 to 1.2 V.

peaks, consistent with the literature [12, 18]. The two quasi-reversible couples were represented by the high-spin iron system, characterized by an approximate formal potential, $E^{0'}_{PB\text{-}PW}$ of 0.167 ± 0.018

V (taken as the average of the anodic and cathodic peak potentials), and the low-spin iron system with an $E^{0'}_{PB-PG}$ of 0.845 ± 0.022 V (n = 3). These formal potentials were similar to those reported by Lundgren et al. [48]. The observed differences were attributed to the electrodes used by the authors (platinum working and NaCl-saturated calomel reference electrodes). In addition, an increase in current can be observed at potentials less than -0.5 V, which is attributed to the extreme reduction of the deepest layers of the polycrystal and its components, initiating its decomposition. The electrochemical parameters were ΔE_{peak} = 184 mV and i_c/i_a = 0.82 for the PB/PW couple and ΔE_{peak} = 128 mV and i_c/i_a = 1.36 for the BG/PB couple. A slightly positive shift in the reduction and oxidation peaks of PB and BG was observed, as declared by Ricci et al. [54], which could be attributed to the different electrode materials or the different nature of the electrode material.

An important electrochemical parameter is surface coverage, which is related to the kinetics of electron transfer between the absorbed compound and the underlying graphite structure, the stability of the sensor, and the type of limitations on the produced current (diffusion-limited or kinetic). This parameter was estimated by equation 8a from the PB/PW couple area in the CV. The surface coverage (Γ) values from 1.9 to 6.2 x 10^{-8} mol cm^{-2} were obtained, which are consistent with values reported in the literature [12]. Fig. 7 shows the dependence of the current intensity (CI) on the scan rate (v) for the different surface coverages. For thinner PB films, i.e., with Γ values ranging from 1.9 to 4.0 x 10^{-8} mol cm^{-2} (olive and magenta curves, respectively), the current intensity increased linearly with the scan rate up to 1 V s^{-1}, indicating adsorption-controlled processes. However, for thicker PB films, especially with Γ values from 5.2 to 6.2 x 10^{-8} mol cm^{-2} (blue and black curves, respectively), linearity is limited to 0.2 V s^{-1}, indicating the existence of diffusion-limited processes at these surface coverage levels. These results indicate that multilayer formation occurs at surface coverages greater than 4.0 x 10^{-8} mol cm^{-2}, and beyond this point, the processes are diffusion-controlled.

The relationship between the intensity of the cathodic current and surface coverage at different scanning speeds is shown in Fig. 8. According to equation 2, the current is proportional to the surface coverage when a monolayer of redox species is formed (according to the Langmuir model). In our case, this behavior was only observed at low scan rates and with surface coverage up to 4.0 x 10^{-4} mol cm^{-4}, which revealed the formation of multiple layers at higher coverage, and from this point on, the Langmuir model was no longer fulfilled.

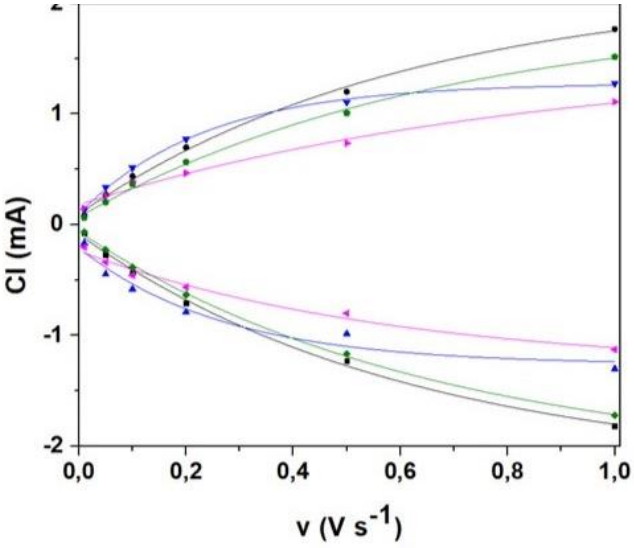

Figure 7. Variation of anodic and cathodic current intensities (CI) with the scan rate (v) at different surface coverages. Γ: 6.2 (black line), 5.2 (blue line), 4.0 (magenta line), and 1.9 (olive line) x 10^{-8} mol cm^{-2}. Solutions in 0.1 mol L^{-1} acetic acid and acetate buffer with 0.1 mol L^{-1} KCl, pH 5.0.

The potentials *vs.* logarithms of the scan rates at different surface coverages are illustrated in Fig. 9, which were used to determine α_a, α_c, and k°. The responses obtained were linearized throughout the study range.

The evaluated values for the α_a and α_c coefficients and the k° calculated from the slope and intercept of Fig. 9 using equations 3, 4, and 5, respectively, are detailed in Table 2. The coefficients are critical parameters in electrochemical studies because they affect the activation energy of electron transfer rate. The value of α (between zero and unity) reflects the symmetry of the free energy curve (concerning the reagents and products). The measured values of aqueous solutions ranged from 0.2 to 0.8, being 0.5 for symmetric curves,

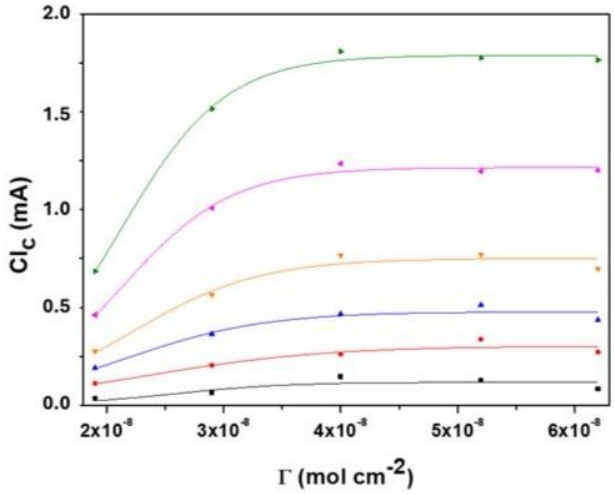

Figure 8. Dependence of CI_c on surface coverages at 0.01 (black line), 0.05 (red line), 0.1 (blue line), 0.2 (orange line), 0.5 (magenta line), and 1 V s^{-1} (olive line). Solutions in 0.1 mol L^{-1} acetic acid and acetate buffer with 0.1 mol L^{-1} KCl, pH 5.0.

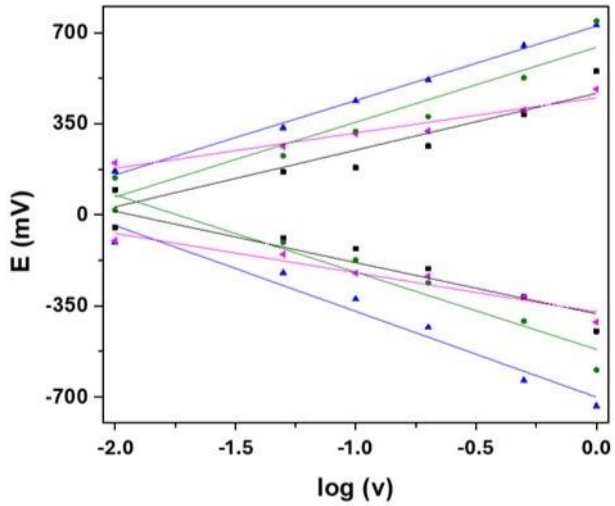

Figure 9. Dependence of E on log (v) at different surface coverages. Surface coverage: 6.2 (black line), 5.2 (blue line), 4.0 (magenta line), and 1.9 (olive line) x 10^{-8} mol cm^{-2}. Solutions in 0.1 mol L^{-1} acetic acid and acetate buffer with 0.1 mol L^{-1} KCl, pH 5.0.

Table 2. Electrochemical characteristics and kinetic data of the PB-cGECE sensor.

Γ (x 10^{-8} mol cm^{-2})	[a]ΔEp (mV)	[a]Ia/Ic	k° (s^{-1})	α_a	α_c
1.9	333	0.92	14	0.31	0.35
4.0	415	0.77	20	0.47	0.51
5.2	558	0.75	13	0.35	0.34
6.2	254	0.98	26	0.76	0.67

[a] Scan rate = 0.05 V s^{-1}

indicating that the activated complex is exactly halfway between the reagents and products on the reaction coordinate [55, 56]. In our study, the sum of the transfer coefficients α_a and α_c was close to its normal value of 1, except in the case of high surface coverage, where the Langmuir model was not satisfied.

On the other hand, k° is an integral parameter for understanding the kinetics of electron transfer processes at the electrode–electrolyte interface. Similar values of k° from 14 to 26 s^{-1} were obtained at different surface coverages, indicating fast electron kinetics and establishment of equilibrium. The reported k° values were 10.7 s^{-1} for hydrogen peroxide on PB-modified graphite electrodes (Γ 5 x 10^{-8} mol cm^{-2}) [18] and ten times lower than 177.9 s^{-1} for ciprofloxacin on a multi-walled nanotube composite film-glassy carbon electrode [19].

3.2. Electrochemical study of quinolones

The electrochemical behaviors of CIP, ENR, DAN, MAR, NOR, OFL, and SAR at 9 000 μg L^{-1} were studied in bare cGECE by cyclic voltammetry (at a scan rate of 0.1 V s^{-1}) in the range from -0.9 to 1.0 V. They demonstrated only small irreversible oxidation peaks at 0.893, 0.814, 0.887, 0.809, 0.880, 0.874, and 0.947 V for CIP, DAN, ENR, MAR, NOR, OFL, and SAR, respectively (Fig. 10). This affirmation is according to the related literature [19, 57].

The electrochemical reaction processes for OFL and CIP oxidation at the surface cGECE can be summarized as shown in Schemes 2A and 2B, respectively [58, 59]. According to the molecular structures (Scheme 3), DAN, ENR, and MAR would have a reaction mechanism like OFL, whereas NOR and SAR would have a mechanism similar to that of CIP. (human use: CIP and NOR; veterinary use: ENR, MAR, DAN, SAR, and OFL).

The working pH is an important parameter for optimizing the sensitivity of detection methods. In this case, the pH of the working buffer was selected considering both the stability of the deposited PB and the electrochemical oxidation of the analytes(quinolone antibiotics). The PB deposited on the electrode reached its highest stability at pH 3.0,

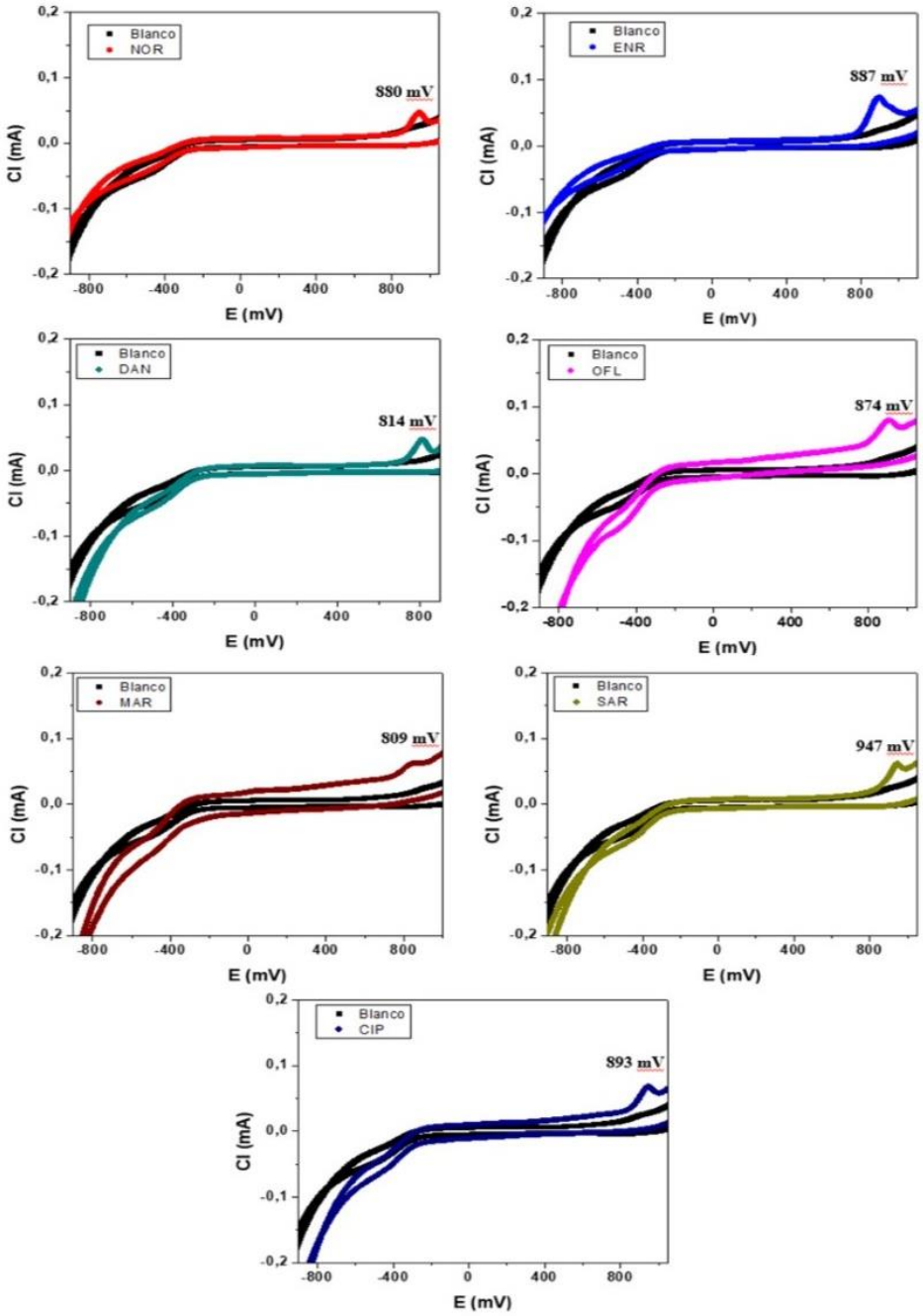

Figure 10. CV recorded on bare cGECE sensor in the absence (black curve) and the presence of 9 000 μg L^{-1} quinolone (colored curves). Solutions in 0.1 mol L^{-1} acetic acid buffer with 0.1 mol L^{-1} KCl at pH 5.0. CV parameters: scan rate 0.1 V s^{-1} and potential range from -0.9 to 1.0 V.

whereas at pH > 7.0, its decomposition started with the formation of $Fe(OH)_3$ [54]. On the other hand, it has been documented that the oxidation of quinolones is favored as the pH increases from 2.0 to 7.0 [19]. Therefore, a compromise pH of 5.0 was selected. Under these conditions, the decomposition of the exposed PB layers would be avoided and, at the same time, the oxidation of the quinolones would be guaranteed.

Fig. 6 shows the cyclic voltammogram of 2 000 μg L^{-1} ENR at the PB-cGECE sensor (voltammogram 3, red curve). The electrocatalytic activity of the immobilized PB toward quinolones is attributed to its

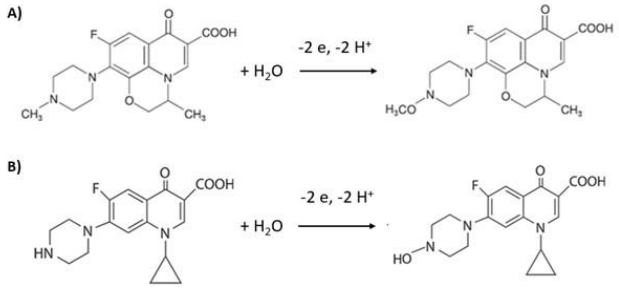

Scheme 2. The electrochemical oxidation mechanisms of OFL (A) and CIP (B).

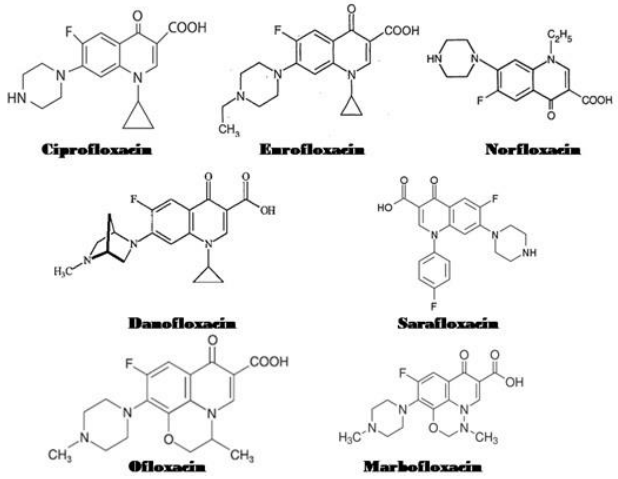

Scheme 3. Chemical structure of the studied quinolones.

zeolitic nature, which acts as a three-dimensional catalyst. Therefore, it can be assumed that this activity could occur both within the immobilized PB and in the surface layers. To understand this, the crystal structure of PB should be considered. Briefly, the crystalline structure of PB is characterized by a 10 Å cubic unit cell with face-centered irons and a 3 Å channel, which allows the diffusion of low molecular mass molecules into the network. The zeolitic lattice has alternating iron ions spaced 5 Å apart, a high-spin iron (with $E^{0'}_{PB\text{-}PW} \approx 0.1$ - 0.2V) and a low-spin iron (with $E^{0'}_{PB\text{-}BG} \approx 0.8$ - 0.95V). In the crystal lattice, 25% of the $[Fe^{II}(CN)_6]^{4-}$ molecules present vacancies occupied by water molecules that are easily displaced by other ligands that can diffuse and react electrochemically. Therefore, these vacancies would contribute to the internal electrocatalytic capacity. On the other hand, the alternating iron ions centered on the faces of the cubic cells are also exposed to interact superficially with electroactive ligands in the external environment [60]. Although quinolones are small molecules (dimensions of 13.5 Å x 3 Å x 7.4 Å for CIP, for example) [61], they would have a low probability of diffusing within the crystal lattice, and their interaction is more likely on the PB surface. This hypothesis is reinforced by considering the chemical structures of quinolone congeners. Quinolones possess functional groups characteristic of this family of antibiotics: a carboxylic group at position 3, a basic piperazinyl (or other N-heterocyclic) ring at position 7 in most congeners and a carbonyl oxygen atom at position 4 (Scheme 4) [62].

The pKa_1 values corresponding to the carboxyl group were between 5.33 and 6.53, whereas the pKa_2 values corresponding to the piperazinic group were between 7.57 and 9.33. In our case, at the working pH, the quinolones were mainly found in the zwitterionic form and behaved as high-affinity ligands, especially toward trivalent cations, such as Fe^{III}. Scheme 4 shows the different modes between coordination of quinolones and metals. In liquid systems, quinolones most frequently coordinate with cations in a bidentate manner, via the deprotonated carboxyl group and the oxygen of the neighboring carbonyl group (I), and they coordinate as bidentate ligands to the carboxyl group (II) or both piperazine nitrogen atoms (III), or as a unidentate ligand via the terminal piperazine nitrogen less frequently. However, in the presence of a solid-liquid interface, as in our case, multiple coordination modes are possible simultaneously.

Although quinolones can coordinate with the cations of the high-spin system, the potential is insufficient to trigger their oxidation and their presence as ligands, hinders the mobility of K^+ ions in the crystal lattice (according to equations 8a and 9a) and electron transfer, resulting in a decrease in the electric current density. In voltammogram 3 of Fig. 6 (red curve), it can be observed that the PB-PW pair decreases in the presence of ENR, confirming this behavior, which has also been reported by other authors [18]. In contrast, in the same voltammogram, the PB-BG couplet increases increased in the presence of ENR, with reductions of 16 μA (at 0.754 V) and 21 μA (at 0.917 V) for the net current of reduction and oxidation, respectively. This suggests that the quinolones are coordinated with low-spin iron ions (corresponding

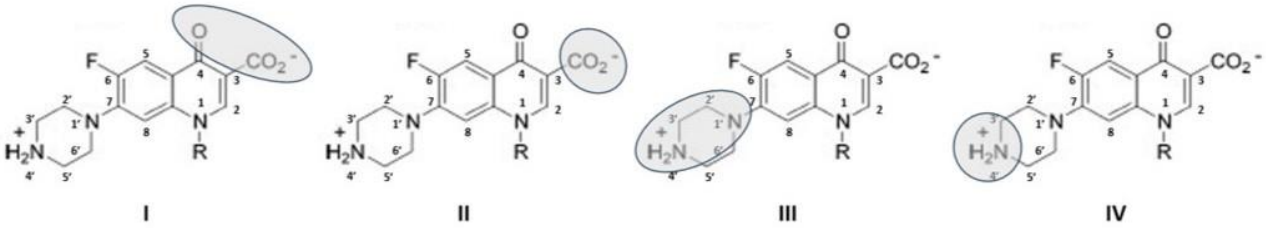

Scheme 4. The different modes of coordination of quinolones with metals.

to the second redox couple in cyclic voltammetry) in the PB film, and that their oxidation is favored under these conditions. The presence of these ligands would favor the diffusion of the ions (K^+ and A^-) into the crystal lattice, resulting in greater catalytic activity. The other tested quinolones exhibited similar behavior. Similar electrocatalytic behavior was also described for hydrazine on a PB-modified glassy carbon electrode [63] and morphine on a PB-modified indium tin oxide electrode [64].

In summary, in the PB film, quinolone is oxidized against BG (oxidized state), which is reduced to the reduced form PB, and subsequently, the electrode reverts to BG, according to the following generic reactions:

Quinolone (QN) oxidation reaction

$$QN_R + H_2O \rightleftharpoons QN_O + 2e + 2H^+ \quad (10)$$

PB oxidation at the cGECE sensor:

$$PB - Xe \rightleftharpoons BG \quad (11)$$

Where, X is the electrode number involved in the reaction, which may vary depending on the form of the PB (soluble or insoluble).

Resulting reaction at the sensor:

$$2BG + XQN_R + XH_2O \rightleftharpoons 2PB + XQN_O + 2XH^+ \quad (12)$$

Therefore, considering the second system (low spin $E_{1/2}$ = 0.845 V vs. ER), it was assumed that the deposited PB film is a mixture of soluble and insoluble forms. In the presence of reduced QN, equations 8b and 9b generate equations 13 and 14, respectively.

$$4K^+ + 6\left[K_{\frac{1}{3}}[Fe^{III}(CN)_6]_{\frac{2}{3}}[Fe^{II}(CN)_6]_{\frac{1}{3}}\right] + 2\,QN_R + 2H_2O \rightleftharpoons 6\,K[Fe^{III}Fe^{II}(CN)_6] + 2\,QN_O + 4\,H^+ \quad (13)$$

$$2\,Fe_4^{III}[Fe^{III}(CN)_6A]_3 + 3\,QN_R + 3\,H_2O \rightleftharpoons 2\,Fe_4^{III}[Fe^{II}(CN)_6]_3 + 6\,H^+ + 6\,A^- + 3\,QN_O \quad (14)$$

After understanding the electrochemical behavior of quinolones on the PB-cGECE sensor, two electrochemical techniques (amperometry and square wave voltammetry) were studied, and the concentration of the precursor liquid mixture for the preparation of PB was optimized.

Previously, the optimum voltage applied in amperometry was ascertained by hydrodynamic voltammetry. This was performed by amperometry in stirred 100 µg L^{-1} ENR solutions by applying increasing potentials at the working electrode in steps of 0.1 V in the anodic branch. The quinolone concentration was approximately 100 times lower than that detected in the bare cGECE sensor (Fig. 10). Therefore, the detection sensitivity of quinolones on the bare cGECE sensor was 100 times lower than that of the PB-cGECE sensor. Fig. 11 shows the dependence of the current on the applied potential for ENR by hydrodynamic voltammetry. The current increased rapidly quickly increases with increasing positive applied potential from 0.8 to 1.0 mV when the maximum current was reached. Hence, 0.95 V *vs.* RE was selected as the applied potential for the following amperometric measurements.

On the other hand, amperometric and voltammetric detections of 300 µg L^{-1} ENR (central zone of the calibration curve, in Fig. 11) were performed at five different concentrations of the precursor mixture ranging from 0.001 to 0.1 mol L^{-1}. The electrochemical techniques assayed were amperometry ($E_{applied}$ = 0.95 V *vs.* RE) and square wave voltammetry (SWV, parameters: step height = 4 mV, amplitude = 25 mV, square-wave frequency = 15 Hz, and potential range = 0.2 - 1.3 V). In Fig. 12, the $K_3[Fe(CN)_6]$: $FeCl_3$ concentrations (1:1) were related to the electrochemical techniques.

The amperometric detection presented higher current intensities than voltammetric detection at precursor

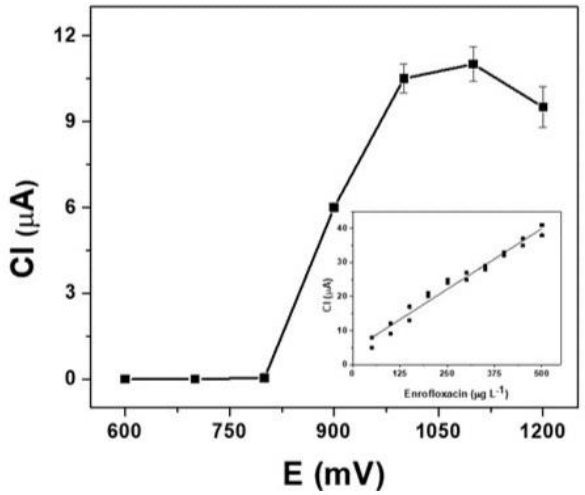

Figure 11. Steady-state current intensity against the applied potential in amperometry for the 100 μg L^{-1} ENR oxidation on PB-cGECE sensor (Γ = 4 x 10^{-8} mol cm^{-2}). The insert graph includes the calibration curve from 25 to 500 μg L^{-1} ENR at 0.95 V *vs.* RE. Solutions in 0.1 mol L^{-1} acetic acid and acetate buffer with 0.1 mol L^{-1} KCl at pH 5.0.

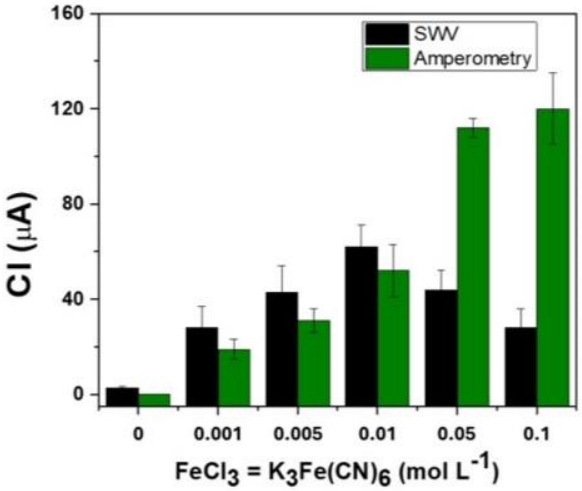

Figure 12. Current intensity *vs.* electrochemical detection technique (SWV or amperometry) for 300 μg L^{-1} ENR at different concentrations of the $K_3[Fe(CN)_6]$: $FeCl_3$ (1: 1) mixture on PB-cGECE sensors (Γ = (1.9 – 6.2) x 10^{-8} mol cm^{-2}]. Solutions in 0.1 mol L^{-1} acetic acid and acetate buffer with 0.1 mol L^{-1} KCl at pH 5.0.

concentrations above 0.05 mol L^{-1}. This concentration corresponds to the condition that favors the development of polycrystalline morphologies, as descripted for the S_3 suspension in Section 3.1.1. Therefore, 0.05 mol L^{-1} of $K_3[Fe(CN)_6]$ and $FeCl_3$ were chosen as the optimum concentrations to form PB, and amperometry was the applied technique for quinolone quantification. At this concentration of the precursor mixture, a Γ of 5.2 x 10^{-8} mol cm^{-2} was generated, corresponding to the formation of a multilayer of PB over the surface electrode.

The chemical deposition of PB generates an excess deposit that can act as a reservoir and provide stability to the sensor, as documented by other authors [12, 54]. In our case, after use, the sensor was stored protected from light at room temperature. Stability was evaluated by daily determination of 50 μg L^{-1} CIP solutions for 5 days. At the end of this period, the sensor lost 21 ± 4% of its original response. We attribute this relative stability to the slightly acidic working pH, which, allowing the oxidation of the quinolones, that did not cause their deposition and decreased the formation of $Fe(OH)_3$.

3.3. Analytical performance

In-house validation assays of the screening method based on the amperometric detection of quinolones in water samples were performed according to the Commission Implementing Regulation (EU) 2021/808 [28].

3.3.1. Calibration curve

The calibration curves for the quantification of the seven quinolones were constructed by amperometric analysis ($E_{applied}$ = 0.95 V *vs.* RE) at seven equidistant levels in triplicate on PB-cGECE sensors. Fig. 13 shows

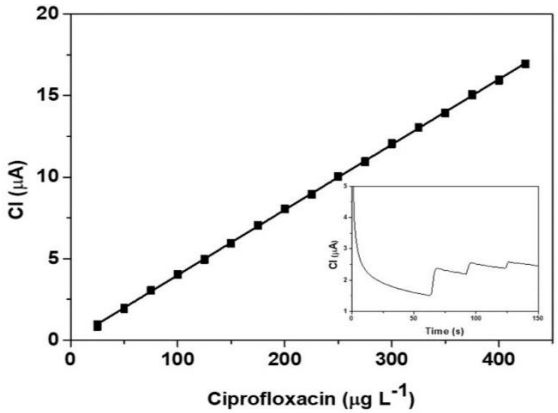

Figure 13. The calibration plots of the oxidation current intensities *vs.* CIP concentrations by amperometry, recorded at $E_{applied}$ = 0.95 V *vs.* RE. The inset graph includes the amperograms recorded on the PB-cGECE sensors and with additions of CIP at 12, 10.25, and 5.2 μg L^{-1} in working buffer at pH = 5.0.

the linear regression from the calibration curve of CIP

as an example, which was adjusted to the equation 15 (R^2 = 0.9998):

$$CI\ (\mu A) = -0.04003\ (\pm 0.00007)(\mu A^{-1}) \times C_{CIP}\ (\mu g\ L^{-1}) + 0.01\ (\pm 0.02)\ (\mu A) \quad (15)$$

Then, the curves were analyzed by OLS calibration because the data presented a homoscedastic distribution. Table 3 presents the analytical parameters for each quinolone.

The highest analytical sensitivity was obtained for CIP detection, with the lowest LOD. The relative standard deviation (RSD %) of the slope was less than 6% in all cases. The performances in the quinolone detections were decreased from CIP > MAR > DAN > ENR = SAR = OFL > NOR. These limits are similar to those reported in the literature [65-67]. In the first study, ENR, sparfloxacin, and fleroxacin were studied by polarographic and voltammetric analyses in formulations and biological fluids [65]. In the second study, three tetracyclines and seven quinolones (NOR, CIP, ENR, flumequine, nalidixic acid, MAR, and DAN) were analyzed in milk by an electrochemical biosensor based on the carbon dioxide production rate and inhibition of sensitive bacteria growth (*Escherichia coli*) [66]. In the third study, CIP, NOR, OFL, and gatifloxacin were detected in serum and tablets using differential pulse voltammetry [67]. However, these limits were lower than those published in earlier studies [19, 68, 69] and slightly higher than those in which CIP was detected by differential pulse voltammetry on a glassy carbon electrode modified with sodium tetraresorcino-latocuprate (II) [70].

3.3.2. Precision

For studying the variability of the methodology, intra-assays and inter-assays were performed for the detection of CIP, DAN, ENR, MAR, NOR, OFL, and SAR at three levels of concentrations (50, 100, and 150 μgL^{-1}) in the working buffer. The results are shown in Table 4.

The intra-assay test was evaluated by multiple analyses (n = 5) in one assay, while the inter-assay was assessed by analysis in three separate analytical runs (n = 15). The intra- and inter-assay precisions expressed as RSD (%) were lower than 20%, which was considered acceptable according to the Manual on Policies and Procedures of the Association of Official Analytical Chemists (AOAC) [71].

3.3.3. Recovery assays

To evaluate the matrix effect of water samples with different degrees of turbidity, recovery tests were performed. For turbidity estimation from a water sample by dissolved organic matter (DOM) determination, the sample absorbances were read at 254 nm ($UV_{254\ nm}$) as per method [72]. Of the ten water samples assayed, three were selected because they had low, medium, and high turbidity, which correspondence to samples 7, 9, and 6 with DOM values of 0.1831, 3.5512, and 6.000, respectively. First, the absence of quinolone in the three samples was corroborated by the method developed (< LODs for seven quinolones). Then, the three samples were spiked with three levels (50, 100, and 150 $\mu g\ L^{-1}$) of seven quinolones. The recovery values (%) are shown in Table 5.

Recoveries from 80% to 133% with RSD lower than 20% were obtained. These results are acceptable according to the Manual of AOAC [71] and confirm the absence of matrix effect for the seven quinolones tested in the water samples with different turbidity values.

3.3.4. Selection of congener

To validate the screening method of quinolone antibiotics, a congener of this class was selected. On the one hand, the calibration curve for CIP had the best analytical performance (higher analytical sensitivity and lowest LOD) and, on the other hand, it is also the most widely prescribed quinolone in our country (Argentina) [73] and the world [74] and, consequently, it is the most detected in Argentine environmental samples [75, 76]. Therefore, CIP was selected as the representative analyte of the quinolone family for screening.

3.3.5. Detection capability (CCβ)

First, the cut-off value (CCβ) for the screening method must be defined. The CCβ is the smallest content of the analyte that can be detected or quantified in a sample with an error probability of β. For this, at least 20 assays were fortified at the ASC level with CIP. The CCβ calculated from equation 6 for CIP in water was 4.0 $\mu g\ L^{-1}$, and it was used for

Table 3. Analytical parameters of the quinolone regression curves.

Quinolone	[a]Analytical sensibility (μg L^{-1})	[b]RSD % (n = 3)	Linearity range (μg L^{-1})	LOQ (μg L^{-1})	LOD (μg L^{-1})
CIP	0.63	0.2	10 – 425	10	3
DAN	0.08	1.1	60 – 425	60	20
ENR	0.08	2.2	90 – 375	90	30
MAR	0.31	1.4	25 – 200	25	10
NOR	0.05	3.2	130 – 425	130	45
OFL	0.09	5.7	100 – 200	100	35
SAR	0.09	2.2	90 – 425	90	30

[a] Analytical sensibility defined as m/Sy where m was a slope and Sy was instrumental noise; [b] RSD% were calculated as (SD/m)*100, where SD was standard deviation of slope.

Table 4. Intra- and inter-assay precision for seven quinolones.

RSD (%)		CIP	DAN	ENR	MAR	NOR	OFL	SAR
[a]Intra-assay (1 day)	50 μg L^{-1}	18	19	19	16	19	19	19
	100 μg L^{-1}	16	11	10	17	18	16	16
	150 μg L^{-1}	10	10	7	16	13	14	12
[b]Inter-assay (3 days)	50 μg L^{-1}	17	18	16	15	18	18	18
	100 μg L^{-1}	16	15	16	19	18	15	16
	150 μg L^{-1}	6	13	14	16	17	16	13

[a] n (is the number of determinations) = 5 and [b] n = 15.

Table 5. Recovery of seven quinolones in water samples.

R% (RSD%, n = 3)		CIP	DAN	ENR	MAR	NOR	OFL	SAR
[a]Sample 6 (μg L^{-1})	50	100(11)	95(20)	117(20)	92(18)	99(19)	117(20)	114(10)
	100	92(13)	107(9)	100(8)	100(16)	103(9)	100(16)	107(9)
	150	100(9)	96(6)	97(10)	100(18)	102(9)	93(15)	104(13)
[b]Sample 7 (μg L^{-1})	50	100(11)	102(9)	108(11)	88(13)	116(5)	117(20)	128(16)
	100	97(8)	107(9)	91(4)	94(9)	103(12)	100(16)	93(20)
	150	97(5)	96(6)	100(5)	100(18)	95(20)	97(9)	96(13)
[c]Sample 9 (μg L^{-1})	50	108(20)	95(20)	92(13)	80(10)	86(18)	133(13)	114(10)
	100	86(9)	121(8)	100(8)	81(11)	112(10)	100(16)	100(9)
	150	90(5)	92(13)	97(10)	100(18)	109(16)	90(15)	109(6)

[a] Lagoon from Sauce, Entre Ríos, Argentina; [b] stream water from Partido de la Costa, Buenos Aires, Argentina; [c] superficial water from Rafaela, Santa Fe, Argentina.

classifying the water samples as non-compliant (> 4.0 μg L^{-1}) and compliant (< 4.0 μg L^{-1}) in quinolone detection. The screening test was used at its maximum performance in terms of detectability as the estimated cut-off level substantially corresponds to the classical LOD.

3.3.6. Selectivity

Selectivity is the ability of a method to distinguish between an analyte and other substances present in the medium [28]. In the evaluation of method selectivity for different quinolone congeners, the CS% values calculated from equation 7 were 100%, 80%, 104%, 103%, 89%, 82%, and 84% for CIP, DAN, ENR, MAR, NOR, OFL, and SAR, respectively. These results indicate that the screening method using CIP as a congener can detect all assayed quinolones.

The interference study was performed by spiking experiments, adding potentially interfering compounds belonging to other families of veterinary antibiotics (tetracycline, β-lactam, macrolide, and sulfonamide families). The recoveries (%) between the response of CIP in the absence and presence of other

Table 6. Interference test in the ciprofloxacin detection at three levels in the presence of other potential interferents at 150 μg L^{-1}

Analytes		Recovery % (RSD%, n = 3)		
		50 μg L^{-1}	100 μg L^{-1}	150 μg L^{-1}
Tetracycline	Doxycycline	75 (15)	87 (6)	85 (12)
β-lactam	Amoxicillin	97 (8)	96 (17)	99 (10)
Macrolide	Azithromycin	84 (5)	87 (15)	90 (12)
	Rifampicin	95 (4)	97 (10)	105 (13)
Sulfonamide	Sulfadimethoxine	76 (14)	81 (10)	87 (16)
	Sulfamethoxazole	72 (20)	80 (18)	84 (19)

antibiotics were calculated and are shown in Table 6. Good recoveries were obtained with values from 72% to 105% with RSD values lower than 20%, which are acceptable values according to the the Manual of AOAC [71]. This indicates that other antibiotic families do not interfere with quinolone class detection.

3.3.7. Water samples

To evaluate the applicability of the method in water samples, ten samples of different origins were analyzed by amperometry on PB-cGECE sensors. Initially, the samples were characterized by analyzing their pH and DOM. The samples had pH values ranging from 6.3 to 8.3, while the DOM values were 0.0023, 0.738, 0.3544, 0.5215, 0.2378, 6.000, 0.1831, 0.7348, 3.5512, and 4.4696 from samples 1 to 10, respectively. After preconditioning, each sample was analyzed using the method developed to evaluate the presence of quinolones. All samples were classified as compliant (responses < 4.0 μg L^{-1} as CIP equivalents), and the results were consistent with the chromatographic reference method.

3.3.8. Matrix effect

Samples were classified as compliant were used to evaluate the matrix effect on quinolone detection. To do these CIP concentrations ranged from 50 to 400 μg L^{-1} were spiked in the working buffer and water samples. The calibration curves of the current intensity (μA) *vs.* CIP concentration (μg L^{-1}) were generated and the data were analyzed by OLS calibration utilizing MATLAB version 7.6.0. (R2008a) [25, 26]. Fig. 14 shows the CIP calibration curves for the different matrices. The slopes, intercepts, and coefficients of determination (R^2) for each curve in the working buffer or water samples are presented in

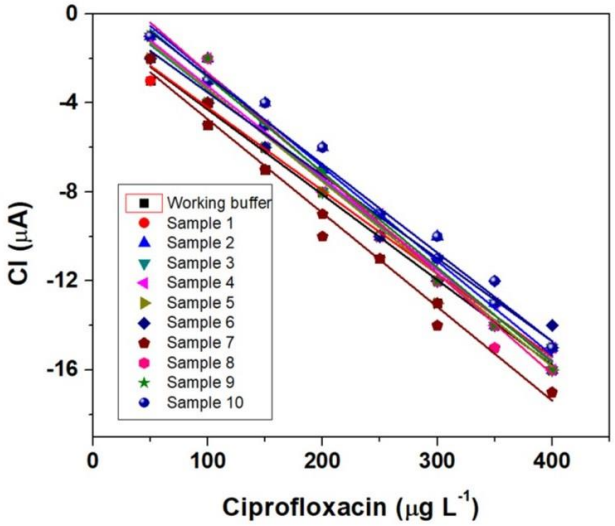

Figure 14. Matrix effect in the CIP detection in the working buffer and in different water samples. Working buffer: 0.1 mol L^{-1} acetic acid and acetate in 0.1 mol L^{-1} KCl, pH 5.0.

Table 7. The slopes in the water matrix ranged from -0.045 to -0.037 μA L $μg^{-1}$ and had no significant differences by Student´s t-test with the buffer matrix ($p > 0.05$), which suggests the absence of matrix effect.

4. Conclusions

The present study indicates that amperometric detection of seven quinolones using the PB-cGECE sensor was successfully performed. The combined results of XRD, Raman, FTIR, UV–Vis, and optical microscopy provided consistent and reproducible evidence of PB formation across all tested precursor concentrations. Higher precursor levels promoted increased crystallinity, larger crystallites, and enhanced optical anisotropy, as reflected by the red shift and broadening of the IVCT band (~700 nm) and the evolution from needle-like morphologies to well-defined cross-like patterns. These correlations

Table 7. Parameters of linear equations of CIP in different matrixes.

[a]Matrix	Slope (μA L μ g^{-1})	Intercept (μ A)	R^2
Working buffer	-0.0383 (± 0.0007)	-0.5 (± 0.2)	0.9898
Sample 1	-0.0374 (± 0.0009)	-0.5 (± 0.2)	0.9916
Sample 2	-0.042 (± 0.001)	1.6 (± 0.3)	0.9835
Sample 3	-0.0405 (± 0.0009)	0.6 (± 0.2)	0.9887
Sample 4	-0.041 (± 0.001)	0.9 (± 0.3)	0.9851
Sample 5	-0.041 (± 0.001)	0.8 (± 0.2)	0.9869
Sample 6	-0.037 (± 0.001)	0.2 (± 0.3)	0.9824
Sample 7	-0.042 (± 0.001)	-0.5 (± 0.3)	0.9857
Sample 8	-0.045 (± 0.001)	1.9 (± 0.3)	0.9866
Sample 9	-0.043 (± 0.001)	1.4 (± 0.3)	0.9866
Sample 10	-0.040 (± 0.001)	1.2 (± 0.3)	0.9841

[a] Working buffer: 0.1 mol L^{-1} acetic acid and acetate in 0.1 mol L^{-1} KCl, pH 5.0. Samples: groundwater (1) and river water (2) from Santo Tome, Santa Fe, Argentina; stream water (3), (4), (5) and lagoon (6) from Sauce, Entre Ríos, Argentina; stream water (7) from Partido de la Costa, Buenos Aires, Argentina; superficial water (8) from Susana, Santa Fe, Argentina; superficial water (9) from Rafaela, Santa Fe, Argentina; and superficial water (10) from San Vicente, Santa Fe, Argentina.

highlight the precursor concentration as a key parameter for tailoring PB's structural and optical properties, and the control of this parameter was used here to ensure the robustness (or repeatability) of the sensor construction. The characterization of the modified electrode was studied by determining different electrochemical parameters such as the electroactive surface coverage (Γ), transfer coefficient (α_a and α_c), and standard heterogeneous rate constant (k°). These results, indicate that the PB-cGECE sensor exhibits good electrocatalytic activity for quinolone oxidation. The times of PB-cGECE sensor preparation and quinolone detection in a water sample were 40 and 5 min, respectively. Calibration curves for the seven quinolones were obtained by amperometry on PB-cGECE sensors with LODs ranging from 3 to 45 μg L^{-1}. Good analytical performances were obtained for the quantitative methods for the seven quinolones, with intra- and inter-assay precisions lower than 20%, and recoveries from 80% to 133% of the seven quinolones in water samples with different degrees of turbidity. CIP was selected as the representative analyte for quinolone family detection, and a CCβ of 4.0 μg L^{-1} was estimated. Good selectivity for the quinolone family was obtained, without the interference of other antibiotic families found frequently in environmental samples (tetracyclines, β-lactam, macrolides, and sulfonamides), and the absence of matrix effect in the CIP detection from water samples. The method could be applied successfully in the quinolone analysis of ten water samples from different origins and with variable amounts of DOM. Future work could explore the miniaturization of portable field-based detection of quinolone residues in environmental water samples.

Disclaimer (artificial intelligence)

Author(s) hereby state that no generative AI tools such as Large Language Models (ChatGPT, Copilot, etc.) and text-to-image generators were utilized in the preparation or editing of this manuscript.

Authors' contributions

Equal contributions of whole study, S.V.K., S.R.H.; characterization studies of PB particles employed in the fabrication of the PB-cGECE sensor, F.A.M.

Acknowledgements

This is not applicable.

Funding

This work was supported by CAI+D 2020 PI 50520190100130LI (UNL), PICT-2022-2022-03-00480 (FONCyT), and CAI+D 2024 85520240100128LI (UNL).

Availability of data and materials

The data used to support the findings of this study can be obtained from the corresponding authors upon

request.

Conflicts of interest

The authors declare no conflict of interest in this reported work.

References

1. Zhang, C.; Wang, H.; Mu, Y.; Liu, H. A method for simultaneously and accurately quantify seven quinolones in matrix reference materials by HPLC-MS. Microchem. J. 2024, 204, 110984. https://doi.org/10.1016/j.microc.2024.110984
2. Suryoprabowo, S.; Nasyiruddin, R.; Wang, Z.; Hendriko, A.; Tristanto, N. A comprehensive review on the pretreatment and detection methods of fluoroquinolones in food and environment. J. Food Comp. Anal. 2025, 140, 107179. https://doi.org/10.1016/j.jfca.2024.107179
3. Yusuf, F.; Ahmed, S.; Dy, D.; Baney, K.; Waseem, H.; Gilbride, K. Occurrence and characterization of plasmid-encoded qnr genes in quinolone-resistant bacteria across diverse aquatic environments in southern Ontario. Can. J. Microbiol. 2024, In Press, Corrected Proof. https://doi.org/10.1139/cjm-2024-0029
4. Hayes, A.; Murray, L.; Stanton, I.; Zhang, L.; Snape, J.; Gaze, W.; et al. Predicting selection for antimicrobial resistance in UK wastewater and aquatic environments: Ciprofloxacin poses a significant risk. Environ. Int. 2022, 169, 107488. https://doi.org/10.1016/j.envint.2022.107488
5. Pu, X.; Wang, X.; Liu, Y.; Di, X. A novel deep eutectic solvent-based ultrasound-assisted dispersive liquid–liquid microextraction coupled with high-performance liquid chromatography for the determination of quinolones in environmental water samples. Microchem. J. 2023, 195, 109374. https://doi.org/10.1016/j.microc.2023.109374
6. Kheirandish, S.; Goudarzi, S.; Amirahmadi, M.; Ghareghani, S.; Ghafari, H.; Daraei, B.; et al. Method validation for simultaneous determination of macrolides, quinolones, and sulfonamides antibiotics in Iranian yogurt samples by SPE clean-up and UHPLC-MS/MS. Microchem. J. 2023, 193, 109103. https://doi.org/10.1016/j.microc.2023.109103
7. Pan, Y.; Yang, V.; Wen, K.; Ke, Y.; Shen, J.; Wang, Z. Current advances in immunoassays for quinolones in food and environmental samples. TrAC, Trends Anal. Chem. 2022, 157, 116726. https://doi.org/10.1016/j.trac.2022.116726.
8. Moreno-González, D.; Hamed, A.; Gilbert-López, B.; Gámiz-Gracia, L.; García-Campaña, A. Evaluation of a multiresidue capillary electrophoresis-quadrupole-time-of-flight mass spectrometry method for the determination of antibiotics in milk samples. J. Chromatogr. A 2017, 1510, 100-107. https://doi.org/10.1016/j.chroma.2017.06.055
9. Zhang, S.; Yu, S.; Wang, X.; Zhang, Y.; Yue, Z.; Li, C.; et al. An electrochemical sensor based on MnO_2/ZnO composites for the detection of ciprofloxacin in honey. Microchem. J. 2023, 194, 109355. https://doi.org/10.1016/j.microc.2023.109355
10. Amine, A.; Mohammadi, H. Amperometry. Encyclopedia of Analytical Science (Third Edition) 2019, 85-98. https://doi.org/10.1016/B978-0-12-409547-2.14204-0
11. Koncki, R. Chemical sensors and biosensors based on prussian blues. Crit. Rev. Anal. Chem. 2002, 32(1), 79-96. https://doi.org/10.1080/10408340290765452
12. Ricci, F.; Palleschi, G. Sensor and biosensor preparation, optimisation and applications of prussian blue modified electrodes. Biosens. Bioelectron. 2005, 21(3), 389-407. https://doi.org/10.1016/j.bios.2004.12.001
13. Kjeldgaard, S.; Dugulan, I.; Mamakhel, A.; Wagemaker, M.; Iversen, B.; Bentien, A. Strategies for synthesis of Prussian blue analogues. R. Soc. Open Sci. 2021, 8(1), 201779. https://doi.org/10.1098/rsos.201779
14. Farah, A.; Billing, C.; Dikio, C.; Dibofori-Orji, A.; Oyedeji, O.; Wankasi, D.; et al. Synthesis of prussian blue and its electrochemical detection of hydrogen peroxide based on cetyltrimethylammonium bromide (CTAB) modified glassy carbon electrode. Int. J. Electrochem. Sci. 2013, 8(11), 12132 – 12146. https://doi.org/10.1016/S1452-3981(23)13250-0
15. Xing, Y.; Wu, G.; Ma, Y.; Yu, Y.; Yuan, X.; Zhu, X. Electrochemical detection of bisphenol B based on poly (Prussian blue)/carboxylated multiwalled carbon nanotubes composite modified electrode. Measurement. 2019, 148, 106940. https://doi.org/10.1016/j.measurement.2019.106940
16. Soares da Cruza, F.; de Souza Paula, F.; Leoni Franco, D.; Torres Pio dos Santos, W.; Franco Ferreira, L. Electrochemical detection of uric acid using graphite screen-printed electrodes modified with prussian blue/poly(4-aminosalicylic acid)/Uricase. J. Electroanal. Chem. 2017, 806, 172-179. https://doi:10.1016/j.jelechem.2017.10.070
17. Rocha, R.; Stefano, J.; Cardoso, R.; Zambiazi, P.; Bonacin, J.; Richter, E.; et al. Electrochemical synthesis of prussian blue from iron impurities in 3D printed graphene

electrodes: Amperometric sensing platform for hydrogen peroxide. Talanta. 2020, 219, 121289. https://doi.org/10.1016/j.talanta.2020.121289

18. Chaves Carvalho, C.; de Andrade Rodrigues, G.; Lopes Magalhães, J.; Alves de Sousa Luz, R.; Santos Gerôncio da Silva, E.; Cantanhêde, W. Effect of Ibuprofen on the electrochemical properties of prussian blue/single-walled carbon nanotubes nanocomposite modified electrode. Surf. Interfaces. 2021, 25, 101276. https://doi.org/10.1016/j.surfin.2021.101276
19. Fotouhi, L.; Alahyari, M. Electrochemical behavior and analytical application of ciprofloxacin using a multi-walled nanotube composite film-glassy carbon electrode. Colloids Surf. B Biointerfaces. 2010, 81(1), 110-114. https://doi.org/10.1016/j.colsurfb.2010.06.030
20. Bard, A.; Faulkner, L.; White, H. Electrochemical methods, in: Fundamentals and Applications, 3rd Edition, Wiley, New York; 2022.
21. Kergaravat, S.; Beltramino, L.; Garnero, N.; Trotta, L.; Wagener, M.; Pividori, M.; et al. Magneto inmunosensor electroquímico para la detección de anticuerpos anti-TG2 en la enfermedad celíaca. Biosens. Bioelectron. 2013, 48, 203-209. https://doi.org/10.1016/j.bios.2013.04.012
22. Pividori, M.; Lermo, A.; Zacco, E.; Hernández, S.; Fabiano, S.; Alegret, S. Bioaffinity platforms based on carbon-polymer biocomposites for electrochemical biosensing. Thin Solid Films. 2007, 516(2-4), 284–292. https://doi.org/10.1016/j.tsf.2007.06.063
23. Zacco, E.; Adrian, J.; Galve, R.; Marco, M..; Alegret, S.; Pividori, M. Electrochemical magneto immunosensing of antibiotic residues in milk. Biosens. Bioelectron. 2007, 22(9-10), 2184-2191. https://doi.org/10.1016/j.bios.2006.10.014
24. Laviron, E. General expression of the linear potential sweep voltammogram in the case of diffusionless electrochemical systems. J. Electroanal. Chem. 1979, 101(1), 19-28. https://doi.org/10.1016/S0022-0728(79)80075-3
25. Eurachem Guide: The Fitness for Purpose of Analytical Methods – A Laboratory Guide to Method Validation and Related Topics, Magnusson, B.; Örnemark, U. (Eds.), 2nd Ed., 2014. www.eurachem.org
26. Raposo, F. Evaluation of analytical calibration based on least-squares linear regression for instrumental techniques: A tutorial review. TrAC-Trend Anal. Chem., 2016, 77, 167-185. https://doi.org/10.1016/j.trac.2015.12.006
27. Validation of Analytical Procedures Q2(R2). International Council for Harmonisation of Technical Requirements for Pharmaceuticals for Human Use, ICH Harmonised Guideline, EMA/CHMP/ICH/82072/2006, 2022.
28. Commission Implementing Regulation (EU) 2021/808 on the performance of analytical methods for residues of pharmacologically active substances used in food-producing animals and on the interpretation of results as well as on the methods to be used for sampling and repealing Decisions 2002/657/EC and 98/179/EC. Off. J. Eur. Union. https://eur-lex.europa.eu/legal-content/EN/TXT/PDF/?uri=CELEX:3; 2021.
29. IRAM 29012-4. Calidad del medio ambiente. Calidad del agua. Muestreo. Parte 4: Directivas para el muestreo de aguas de lagos naturales y artificiales. https://www.iram.org.ar/busqueda-avanzada-de-normas-iram/, 1997.
30. IRAM 29012-5. Calidad del medio ambiente. Calidad de agua. Muestreo. Parte 5: Guía sobre muestreo de agua potable y de aguas utilizadas para el procesamiento de alimentos y bebidas. https://www.iram.org.ar/busqueda-avanzada-de-normas-iram/, 1998.
31. IRAM 29012-6 Calidad ambiental - Calidad del agua. Muestreo. Parte 6 - Directivas para el muestreo de ríos y arroyos. https://www.iram. org.ar/busqueda-avanzada-de-normas-iram/, 2019.
32. IRAM 29012-11 Calidad ambiental. Calidad de agua - Muestreo. Parte 11: Directivas para el muestreo de aguas subterráneas. https://www.iram.org.ar/busqueda-avanzada-de-normas-iram/; 1999.
33. da Silva, D.; Oliveira C. Development of micellar HPLC-UV Method for determination of pharmaceuticals in water samples. J. Anal. Methods Chem. 2018, 1471, 1-12. https://doi.org/10.1155/2018/9143730
34. Parma, M.; Beraldo, H.; de Castro Mendes, I. Syntheses of prussian blue pigment following 18th-century methodologies: Factors influencing product purity and syntheses yields. ACS Omega. 2025, 10, 11375-11385. https://doi.org/10.1021/acsomega.4c11328
35. Shiba, F.; Mameuda, U.; Tatejima, S.; Okawa, Y. Synthesis of uniform prussian blue nanoparticles by a polyol process using a polyethylene glycol aqueous solution. RSC Adv. 2019, 9, 34589-34594. https://doi.org/10.1039/C9RA07080J
36. Farah, A.; Shooto, N.; Thema, F.; Modise, J.; Dikio, E. Fabrication of prussian blue/multi-walled carbon nanotubes modified glassy carbon electrode for electrochemical detection of hydrogen peroxide. Int. J. Electrochem. Sci. 2012, 7, 4302-4313. https://doi.org/10.1016/S1452-3981(23)19539-3
37. Jadoun, S.; Arif, R.; Jangid, N.; Meena, R. Green synthesis of nanoparticles using plant extracts: a review. Environ. Chem. Lett. 2021, 19, 355-374.

https://doi.org/10.1007/s10311-020-01074-x
38. Buser, H.; Ludi, A.; Schwarzenbach, D.; Petter, W. The crystal structure of prussian blue: $Fe_4[Fe(CN)_6]_3.xH_2O$. Inorg. Chem. 1977, 16(11), 2704-2710. https://doi.org/10.1021/ic50177a008
39. Baggio, B.; Vicente, C.; Pelegrini, S.; Cid, C.; Brandt, I.; Tumelero, M.; *et al.* Morphology and structure of electrodeposited prussian blue and prussian white thin films. Materials. 2019, 12(7), 1103. https://doi.org/10.3390/ma12071103
40. Wang, N.; Ma, W.; Du, Y.; Ren, Z.; Han, B.; Zhang, L.; et al. Prussian blue microcrystals with morphology evolution as high-performance photo-fenton catalyst for degradation of organic pollutants. ACS Appl. Mater. Interfaces. 2019, 11(1), 1174–1184. https://pubs.acs.org/doi/abs/10.1021/acsami.8b14987
41. Moretti, G.; Gervais, C. Raman spectroscopy of the photosensitive pigment Prussian blue. Raman Spectrosc. 2018, 49, 1198-1204. https://doi.org/10.1002/jrs.5366
42. Orlando, A.; Franceschini, F.; Muscas, C.; Pidkova, S.; Bartoli, M.; Rovere, M.; et al. A comprehensive review on raman spectroscopy applications. Chemosensors. 2021, 9(9), 262. https://doi.org/10.3390/chemosensors9090262
43. Dai, F.; Zhuang, Q.; Huang, G.; Deng, H.; Zhang, X. Infrared spectrum characteristics and quantification of OH groups in coal. ACS Omega. 2023, 8(19), 17064-17076. https://doi.org/10.1021/acsomega.3c01336
44. Rohilla, S.; Lal, B.; Sunder, S.; Aghamkar, P.; Kumar, S.; Aggarwal, A. synthesis of $Fe_4[Fe(CN)_6]_3{\cdot}14H_2O$ nanopowder by co-precipitation technique and effect of heat treatment. Acta Phys. Pol. A 2010, 118(4), 696-700. https://doi.org/10.12693/APhysPolA.118.696
45. Dumani, D.; Cook, J.; Kubelick, K.; Luci, J.; Emelianov S. Photomagnetic prussian blue nanocubes: synthesis, characterization, and biomedical applications. Nanomedicine. 2020, 24, 102138. https://doi.org/10.1016/j.nano.2019.102138
46. Giacomo Dacarro, G.; Taglietti, A.; Pallavicini, P. Prussian blue nanoparticles as a versatile photothermal tool, Molecules. 2018, 23(6), 1414. https://doi.org/10.3390/molecules23061414
47. Ricci, F.; Moscone, D.; Palleschi, G. Procedure 17 preparation of prussian blue-modified screen-printed electrodes via a chemical deposition for mass production of stable hydrogen peroxide sensors. Comprehensive Anal. Chem. 2007, 49, e119-e124. https://doi.org/10.1016/S0166-526X(06)49060-7
48. Lundgren, C.; Murray, R. Observations on the composition of prussian blue films and their electrochemistry. Inorg. Chem. 1988, 27 (5), 933-939. https://doi.org/10.1021/ic00278a036
49. Keggin, J., Miles, F. Structures and formulae of the prussian blues and related compounds. Nature. 1936, 137, 577–578. https://doi.org/10.1038/137577a0
50. Ellis, D.; Eckholf, M.; Neff, V. Electrochromism in the mixed-valence hexacyanides. 1. voltammetric and spectral studies of the oxidation and reduction of thin films of prussian blue. Phys. Chem. 1981, 85(9), 1225-1231. https://doi.org/10.1021/j150609a026
51. Itaya, K.; Ataka, T.; Toshima, S. Spectroelectrochemistry and electrochemical preparation method of prussian blue modified electrodes. J. Am. Chem. Soc. 1982, 104(18), 4767 – 4772. https://doi.org/10.1021/ja00382a006
52. Itaya, K.; Uchida, I.; Neff, V. Electrochemistry of polynuclear transition metal cyanides: Prussian blue and its analogues. Acc. Chem. Res. 1986, 19(6), 162-168. https://doi.org/10.1021/ar00126a001
53. Cretu, R.; Gligor, D.; Muresan, L.; Popescu, I.; Muresan, L. Kinetic characterization of prussian blue-modified graphite electrodes for amperometric detection of hydrogen peroxide. J. Appl. Electrochem. 2006, 36(12) 1327-1332. https://doi.org/10.1007/s10800-006-9242-8
54. Ricci, F.; Amine, A.; Palleschi, G.; Moscone, D. Prussian blue based screen printed biosensors with improved characteristics of long-term lifetime and pH stability. Biosens. Bioelectron. 2003, 18(2-3), 165-174. https://doi.org/10.1016/s0956-5663(02)00169-0
55. Wang J. Analytical Electrochemistry. Second Edition. Wiley-VHC. New York, EE.UU. 2011.
56. Masood, Z.; Muhammad, H.; Tahiri, I. Comparison of different electrochemical methodologies for electrode reactions: A case study of paracetamol. Electrochem. 2024, 5, 57–69. https://doi.org/10.3390/Electrochem5010004
57. Adane, W.; Chandravanshi, B.; Tessema, M. A simple, ultrasensitive and cost-effective electrochemical sensor for the determination of ciprofloxacin in various types of samples. Sens. Bio-Sens. Res. 2023, 39, 100547. https://doi.org/10.1016/j.sbsr.2022.100547
58. Si, X.; Bai, C.; Gong, X.; Han, J.; Chen, Z.; Ding, Y. Detection of ofloxacin by differential pulse voltammetry in drugs based on a novel p-aminobenzene sulfonic acid/graphene electrochemical sensor. Int. J. Electrochem. Sci. 2020, 15, 8883–8891. https://doi.org/10.20964/2020.07.46
59. Jiwanti, P.; Sukardi, D.; Sari, A.; Tomisaki, M.; Wafiroh, S.; Hartati, S.; et al. Fabrication and characterization of rGO-SnO2 nanocomposite for electrochemical sensor of ciprofloxacin. Sens. Int. 2024, 5, 100276. https://doi.org/10.1016/j.sintl.2023.100276
60. Khasevani, S.; Nikjoo, D.; Ojwang, D.; Nodari,

L.; Sarmad, S.; Mikkola, J.; et al. The beauty of being complex: Prussian blue analogues as selective catalysts and photocatalysts in the degradation of ciprofloxacin. J. Catal. 2022, 410, 307–319. https://doi.org/10.1016/j.jcat.2022.04.029

61. Carabineiro, S.; Thavorn-amornsri, T; Pereira, M.; Serp, P.; Figueiredo, J.; Comparison between activated carbon, carbon xerogel and carbon nanotubes for the adsorption of the antibiotic ciprofloxacin. Catalysis Today. 2012, 186(1), 29-34. https://doi.org/10.1016/j.cattod.2011.08.020
62. Uivarosi, V. Metal complexes of quinolones antibiotics and their applications: An uptate. Molecules. 2013, 18, 11153-11197. https://doi.org/10.3390/molecules180911153
63. Hou, W.; Wang, E. Flow-injection amperometric detection of hydrazine by electrocatalytic oxidation at a Prussian Blue film-modified electrode. Anal. Chim. Acta. 1992, 257(2), 275-280. https://doi.org/10.1016/0003-2670(92)85180-E
64. Ho, K.; Chen, C.; Hsu, H.; Chen, L.; Shiesh, S.; Lin, X. Amperometric detection of morphine at a Prussian blue-modified indium tin oxide electrode. Biosens. Bioelectron. 2004, 20(1), 3-8. https://doi.org/10.1016/j.bios.2003.11.027
65. Rizk, M.; Belal, F.; Ibrahim, F.; Ahmed, S.; EL-Enany, N. Voltammetric analysis of certain 4-quinolones in pharmaceuticals and biological fluids. J. Pharmaceut. Biomed. 2000, 24(2), 211-218. https://doi.org/110.1016/s0731-7085(00)00401-5
66. Pellegrini, G.; Carpico, G.; Coni, E. Electrochemical sensor for the detection and presumptive identification of quinolone and tetracycline residues in milk. Anal. Chim. Acta 2004, 520(1-2), 13-18. https://doi.org/10.1016/j.aca.2004.04.052
67. Zhang, F.; Gu, S.; Ding, Y.; Zhang, Z.; Li, L. A novel sensor based on electropolymerization of b-cyclodextrin and L-arginine on carbon paste electrode for determination of fluoroquinolones. Anal. Chim. Acta 2013, 770, 53–61. https://doi.org/10.1016/j.aca.2013.01.052
68. Shitahun, A.; Atlabachew, M.; Aragaw, B.; Benor, A.; Metto, M.; Abebe, A. Synthesis, characterization, and application of a novel electrochemical sensor based on poly [Mn(Chr)$_3$]Cl$_2$/PGE for the determination of ciprofloxacin in pharmaceuticals and urine samples. Int. J. Electrochem. Sci. 2025, 20, 100937. https://doi.org/10.1016/j.ijoes.2025.100937
69. Feng, X.; Wang, K.; Song, K.; Han, G.; Li, B.; Kraatz, H. Simultaneous detection of moxifloxacin and gatifloxacin by Cu-TCPP/rGO electrochemical sensor. 2024, 207, 112140. https://doi.org/10.1016/j.microc.2024.112140
70. Kassa, A.; Shitaw, D.; Bitew, Z.; Abebe, A. Eco-friendly electrochemical sensing: An ultra-sensitive voltametric analysis of ciprofloxacin in human serum, cow's milk and pharmaceutical samples using a glassy carbon electrode modified with poly(Na$_2$[Cu(HR)$_4$]). Sens. Bio-Sens. Res. 2025, 49, 100825. https://doi.org/10.1016/j.sbsr.2025.100825
71. AOAC, Guidelines for standard method performance requirements, appendix F, https://www.aoac.org/resources/guidelines-for-standard-method-performance-requirements/ 2016
72. Kergaravat, S.; Althaus, R.; Hernández, S. Screening fluorescent method for the fluoroquinolone family in groundwater samples from intensive livestock production systems. J. Environ. Anal. Chem. 2018, 98(11), 1-17. https://doi.org/10.1080/03067319.2018.1520227
73. Boni, S.; Marin, G.; Campaña, L.; Marin, L.; Risso-Patrón, S.; Marin, G.; et al. Association between consumption of fluoroquinolones and carbapenems and their resistance rates in pseudomonasaeruginosa in Argentina.Interdiscip. Perspect. Infect. Dis. 2022, 924212, 1-7. https://doi.org/10.1155/2022/3924212
74. Zou, M.; Tian, W.; Zhao, J.; Chu, M.; Song, T. Quinolone antibiotics in sewage treatment plants with activated sludge treatment processes: A review on source, concentration and removal. Process Saf. Environ. 2022, 160, 116-129. https://doi.org/10.1016/j.psep.2022.02.013
75. Mastrángelo, M.; Valdés, M.; Eissa, B.; Ossana, N.; Barceló, D.; Sabater, S.; *et al.* Occurrence and accumulation of pharmaceutical products in water and biota of urban lowland rivers. Sci. Total Environ. 2022, 828, 154303. https://doi.org/10.1016/j.scitotenv.2022.154303
76. Teglia, C.; Gutierrez, F.; Machado, S.; Hadad, H.; Maine, M.; Goicoechea, H. Spatial occurrence of emerging contaminants in rivers and wastewater. Analysis of environmental and human risks. Environ. Toxicol. Chem. 2025, 44(2), 397–409. https://doi.org/10.1093/etojnl/vgae075